

1 **Assessing Typhoon Soulik-induced morphodynamics over the Mokpo coast region in**
2 **South Korea based on a geospatial approach**

3 Sang-Guk Yum¹, Moon-Soo Song², Manik Das Adhikari^{3*}

4
5 ¹ Department of Civil Engineering, Gangneung-Wonju National University, Gangneung, Gangwon-
6 do 25457, South Korea; skyeom0401@gwnu.ac.kr

7 ² Department of Safety & Disaster Prevention Engineering, Kyungwoon University, Gumi,
8 Gyeongsangbuk-do 39160, South Korea; songms0722@ikw.ac.kr

9 ³ Department of Civil Engineering, Gangneung-Wonju National University, Gangneung, Gangwon-
10 do 25457, South Korea; rsgis.manik@gmail.com

11

12 *Correspondence to: Manik Das Adhikari (rsgis.manik@gmail.com)*

13

14 **Abstract**

15 The inner shelf and coastal region of the Yellow Sea along the Korean peninsula are frequently
16 impacted by Typhoons. The Mokpo coastal region in South Korea was significantly affected
17 by typhoon Soulik in 2018, the deadliest typhoon strike to the southwestern coast since Maemi
18 in 2003. Typhoon Soulik overran the region, causing extensive damage to the coast, shoreline,
19 vegetation, and coastal geomorphology. Therefore, it is important to investigate its impact on
20 the coastal ecology, landform, erosion/accretion, suspended sediment concentration (SSC) and
21 associated coastal changes along the Mokpo region.

22 In this study, net shoreline movement (NSM), normalized difference vegetation index
23 (NDVI), fractional vegetation coverage (FVC), coastal landform change model, normalized
24 difference suspended sediment index (NDSSI), and SSC-reflectance relation have been used
25 to analyze the coastal morphodynamics over the typhoon periods. We used pre-and post-
26 typhoon Sentinel-2B MSI images for mapping and monitoring the typhoon effect and recovery
27 status of the Mokpo coast through short and medium-term coastal change analysis. The
28 findings highlighted the significant impacts of typhoons on coastal dynamics, wetland
29 vegetation and sediment resuspension along the Mokpo coast. It has been observed that
30 typhoon-induced SSC influences shoreline and coastal morphology. The outcome of this
31 research may provide databases to manage coastal environments and a long-term plan to restore
32 valuable coastal habitats. In addition, the findings may be useful for post-typhoon emergency
33 response, coastal planners, and administrators involved in the long-term development of human
34 life.

35

36 **Keywords:** Typhoon Soulik, Coastal changes, NDVI, FVC, Suspended sediment movement,

38 **1. Introduction**

39 Typhoons are one of the most destructive natural calamities. Strong winds that accompany
40 typhoons damage the environment, coastline, wildlife, people, and public and private properties
41 in coastal and inland areas during landfall (Shamsuzzoha et al., 2021; Xu et al., 2021; Mishra
42 et al., 2021a; Nandi et al., 2020; Sadik et al., 2020; Sahoo and Bhaskaran, 2018; Hoque et al.,
43 2016). Many coastal and near-coastal countries are plagued by typhoon-induced storms,
44 flooding, deforestation, and increased soil salinity (Rodgers et al., 2009). Typhoons (tropical
45 cyclones) have caused 1,942 disasters in the past 50 years, resulting in 779,324 fatalities and
46 USD 1,407.6 billion in economic losses worldwide (WMO, 2020), demonstrating their effects
47 on both the global and regional economies (Bhuiyan and Dutta, 2012; Mallick et al., 2017).
48 The effects of typhoons include saltwater intrusion, soil fertility depletion, reduced agricultural
49 productivity, life losses, coastline erosion, vegetation damage, and massive economic disasters
50 (Mishra et al., 2021b).

51 According to instrumental data collected since 1904, typhoon intensity on the Korean
52 peninsula has grown during the previous 100 years (Yu et al., 2018; Cha et al., 2021). A total
53 of 188 typhoons, about three annually, have affected the coastal region from 1959 to 2018
54 (KMA, 2018). Among past Typhoons, RUSA (2002), MAEMI (2003), NARI (2007), and
55 SOULIK (2018) heavily affected the southwestern coast, causing extensive damage to lives
56 and properties (KMA, 2011; 2018). Furthermore, people living in these regions have faced
57 serious coastal floods caused by these events for more than a half-century (Moon et al., 2003).
58 Mokpo coastal region, located in the southwest coast of South Korea, has been hit by 58
59 typhoons since 1980, with most occurring in the July to October period (Kang et al., 2020; Lee
60 et al., 2022). The rapid growth of coastal economies and populations in recent years has made
61 these areas more susceptible to typhoon disasters. Therefore, the increasing frequency of
62 typhoons on the southwestern coasts is a significant issue for disaster management.

63 Several studies (Halder and Bandyopadhyay, 2022; Wang et al., 2021; Shamsuzzoha et
64 al., 2021; Kumar et al., 2021; Sadik et al., 2020; Konda et al., 2018; Parida et al., 2018; Zhang
65 et al., 2013; Yin et al., 2013; Li and Li., 2013; Rodgers et al., 2009) have been carried out in
66 South Asia using various techniques to map the hazard, vulnerability, risk and effects of
67 typhoon disasters. Remote sensing and geospatial technology play a crucial role in monitoring
68 a variety of natural disasters (Wang and Xu, 2018; Mishra et al., 2021b; Charrua et al., 2021).

69 The majority of studies on typhoon-induced coastal dynamics rely on passive optical remote
70 sensing and identify natural disaster damage using changes in landuse data, vegetation indices,
71 and geospatial techniques (Mishra et al., 2021a; Xu et al., 2021; Nandi et al., 2020). The post-
72 typhoon damage assessment research in South Korea mostly focused on property loss,
73 economic losses, and casualties (Yum et al., 2021; Kim et al., 2021; Hwang et al., 2020).
74 However, the coastal morphodynamics along the Mokpo coast over the typhoon period (such
75 as short and medium term) have not been investigated in detail. Thus, this study's primary focus
76 is to determine the effects of typhoon Soulik on coastal ecology, landforms, erosion/accretion,
77 suspended sediment movement and associated coastal changes along the Mokpo coast.

78 The normalized difference vegetation index (NDVI) and variations in NDVI (Δ NDVI)
79 have been used to map the extent of vegetation destruction and details on the degree of damage
80 after the typhoon (Wang et al., 2010; Datta & Deb, 2012; Zhang et al., 2013; Kumar et al.,
81 2021; Xu et al., 2021). Vegetation damage can be seen by the negative change in NDVI values
82 between the post-and pre-typhoon period (Mishra et al., 2021a; Hu and Smith, 2018). On the
83 other hand, fractional vegetation coverage (FVC) is a crucial quantitative indicator of the
84 vegetation cover of the land surface (Zhang et al., 2021; Wang and Xu, 2018; Song et al.,
85 2017). Therefore, FVC has also been used to assess the extent of vegetation damage caused by
86 typhoon Soulik and to analyze its impact on vegetation cover. The coastline movement over
87 the typhoon periods has been analyzed using the Digital Shoreline Analysis System (DSAS)
88 program (Tsai, 2022; Adhikari et al., 2021; Bishop-Taylor et al., 2021; Santos et al., 2021). In
89 order to monitor and protect coastal habitats, we need to understand the distribution and
90 movement of SSC between rivers and coastal waters. Thus, the normalized difference
91 suspended sediment index (NDSSI) (Kavan et al., 2022; Shahzad et al., 2018; Hossain et al.,
92 2010) and the SSC-reflectance algorithm developed by Choi et al. (2014) for the Mokpo coastal
93 region have been used to monitor SSC distribution. Furthermore, to understand the short and
94 medium-term morphodynamics of the coastal landform due to the typhoon, a GIS-based coastal
95 change model has been developed. Four coastal landform classes, i.e., tidally influenced land
96 (wetland land, wetland vegetation) and non-tidally influenced land (land and water), have been
97 used for the coastal morphodynamic analysis (Maiti and Bhattacharya, 2011). The change
98 detection technique has been employed to quantify the short and medium-term coastal changes.
99 This approach focuses on details of morphological changes within the coast and highlights the
100 minor changes caused by the typhoon.

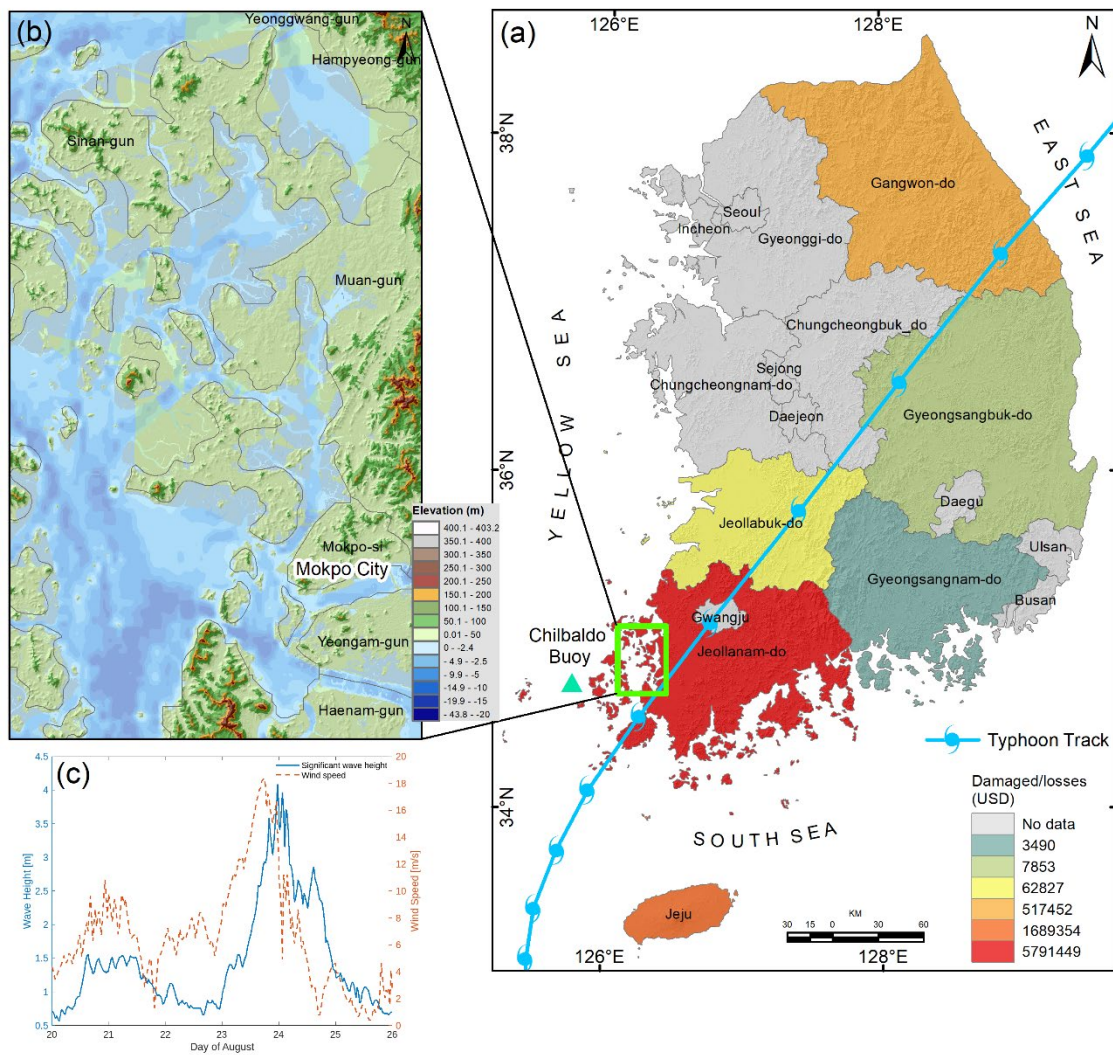
101 This study uses Sentinel-2 MSI images as a primary data source to examine the

102 morphodynamics and effects of Typhoon Soulik on coastal ecology. Accordingly, the
103 objectives of this study are to (i) quantify and mapping of coastal landform dynamics prior to
104 and after the typhoon, (ii) examine shoreline movement and assess coastal erosion and
105 accretion, (iii) assess the degree of typhoon damage to vegetated land, and (iv) analyze changes
106 in SSC and the response of sediment dynamics over the typhoon period. Coastal managers can
107 use this study to develop and implement appropriate strategies and practices to protect natural
108 ecosystems and post-disaster rehabilitation.

109 **2. Study Area**

110 The Mokpo coast is located in the southwestern part of South Korea and is characterized by
111 muddy flats with wide tidal ranges (Choi et al., 2007; Kang et al., 2007), as depicted in Figure
112 1. The inner part of the coast includes harbor and industrial complexes, a large residential area,
113 and a wastewater treatment plant. Mokpo coast is most frequently hit by typhoons, which cause
114 the most significant amount of property damage and loss of human lives (Kang et al., 2020;
115 Lee, 2014). According to storm surge records, the Mokpo coastal region has experienced the
116 highest number of typhoons (58) since 1980 due to its geographical location (Lee et al., 2022;
117 Kang et al., 2020). The tidal range has been observed to be broader, with the extreme high tide
118 60cm higher and the extreme low tide 43cm lower in the Mokpo coast (Lee et al., 2022; Kwon
119 et al., 2018). This fluctuation resulted in significant flooding during the typhoon period. High
120 water and waves severely damage the coastal structures and environment, especially during
121 surges (Tsai et al., 2006). The Mokpo coastal region is characterized by a strong ebb dominant
122 pattern because of its complex bathymetry, scattered islands and extensive tidal flats (Byun et
123 al., 2004; Kang and Jun, 2003; Kang, 1999).

124 The vast tidal flat of the Mokpo coast serves as a habitat for many different species, has
125 a large production capacity, and is highly regarded for its role in cleaning up pollution and
126 controlling floods and typhoons (Lee et al., 2021; Na, 2004). Furthermore, the powerful storm
127 has affected the coastal wetlands (mudflats) that serve as the primary spawning and nursery
128 grounds for fish and other marine life. However, Choi (2014) observed that tidal flat systems
129 in the Korean peninsula are actively responding to various phenomena, such as tides, waves,
130 and typhoons. The wetland, coastal vegetation and coastline along the Mokpo coastal region
131 have been disturbed due to the extreme climatic events. It has been observed that most typhoon
132 passages severely impacted the tidal flat environment and caused morphodynamics along the
133 Mokpo coast.



134

135 Figure 1. (a) Typhoon Soulik passage passed through the Mokpo coastal region on 23rd August
 136 2018 (Typhon track data were downloaded from [https://www.ncdc.](https://www.ncdc.noaa.gov/ibtracs/)
 137 [noaa.gov/ibtracs/](https://www.ncdc.noaa.gov/ibtracs/)), while the background shades represent province-wise recorded
 138 damaged/loss distribution reported by Member Report (2018), (b) Topography
 139 variation of the Mokpo coastal region (elevation data acquired from NGII (2018),
 140 <https://www.ngii.go.kr/>, and bathymetry data downloaded from GMRT,
 141 <https://www.gmrt.org/>), and (c) Variation of significant wave height and wind speed
 142 from August 20 to 25, 2018 recorded by Chilbaldo Buoy Station (located near the
 143 landfall area) during the typhoon Soulik (Data source:
 144 <http://wink.kiost.ac.kr/map/map.do#>).

145

146

147 2.1 Typhoon Soulik

148

149 The southwestern coast of the Korean peninsula was ravaged by the strong intensity
 150 typhoon Soulik, which hit the Mokpo coast on 23rd August 2018 (Ryang et al., 2021). On 16th
 151 August, it developed near Palau as a tropical depression. Subsequently, it strengthened into a
 tropical storm before intensifying into a typhoon (Lee et al., 2022). It moved into the East China

152 Sea on 20th August with a maximum intensity of 950 hPa (44 m/s) and lasted until 22nd August.
153 The Korea Meteorological Administration (KMA) issued typhoon warnings, and national and
154 local authorities took preventative measures to limit potential damage. On 23rd August, around
155 14 UTC, Typhoon Soulik made landfall close to Mokpo city, located on Korea's southwest
156 coast. The typhoon remained on the mainland for an additional 12 hours before moving to the
157 East Sea, where it underwent a transformation and became an extra-tropical cyclone. A peak
158 sustained wind speed of 30.2 m/s was recorded at Gageodo in South Jeolla Province, while the
159 central pressure of the typhoon was measured at 975 hPa (Member Report, 2018). Meanwhile,
160 the strongest gust was observed at Mt. Halla, with a peak gust of 62 m/s. It also dumped
161 tremendous rain (Kang and Moon, 2022; Kang et al., 2020; Yu et al., 2018; Cha et al., 2021).
162 The buoy station near Jeju Island has recorded extreme sea surface conditions, including a
163 maximum wave height of 15m, gusts of 35 m/s, and a drop in water temperature of 10°C. (Kang
164 et al., 2020; Yoon et al., 2021). Figure 1(c) illustrates the variations in sea surface parameters
165 between August 20 and August 25, 2018, in the vicinity of the landfall region (Chilbaldo buoy),
166 including wind speed and significant wave height. It was observed that a significant wave
167 height, i.e., 4-6 m, was recorded at Chilbaldo Buoy station. According to the Ministry of the
168 Interior and Safety (MOIS), typhoon Soulik caused various damages and disruptions across
169 various regions in the country. One woman was reported missing in the coastal area of Jeju,
170 and three people sustained injuries. A total of 362 facilities were damaged. In addition, the
171 typhoon resulted in power outages for 26,830 houses and flooding that affected over 3,063
172 hectares of farmland (Member Report, 2018). Furthermore, the typhoon destroyed extensive
173 vegetation with strong gusts and damaged non-residential structures along the Mokpo coast. A
174 province-wise breakdown of the damage and losses caused by the typhoon is depicted in Figure
175 1(a). The total damage caused by Typhoon Soulik in South Korea was \$45 million (KMA,
176 2018).

177

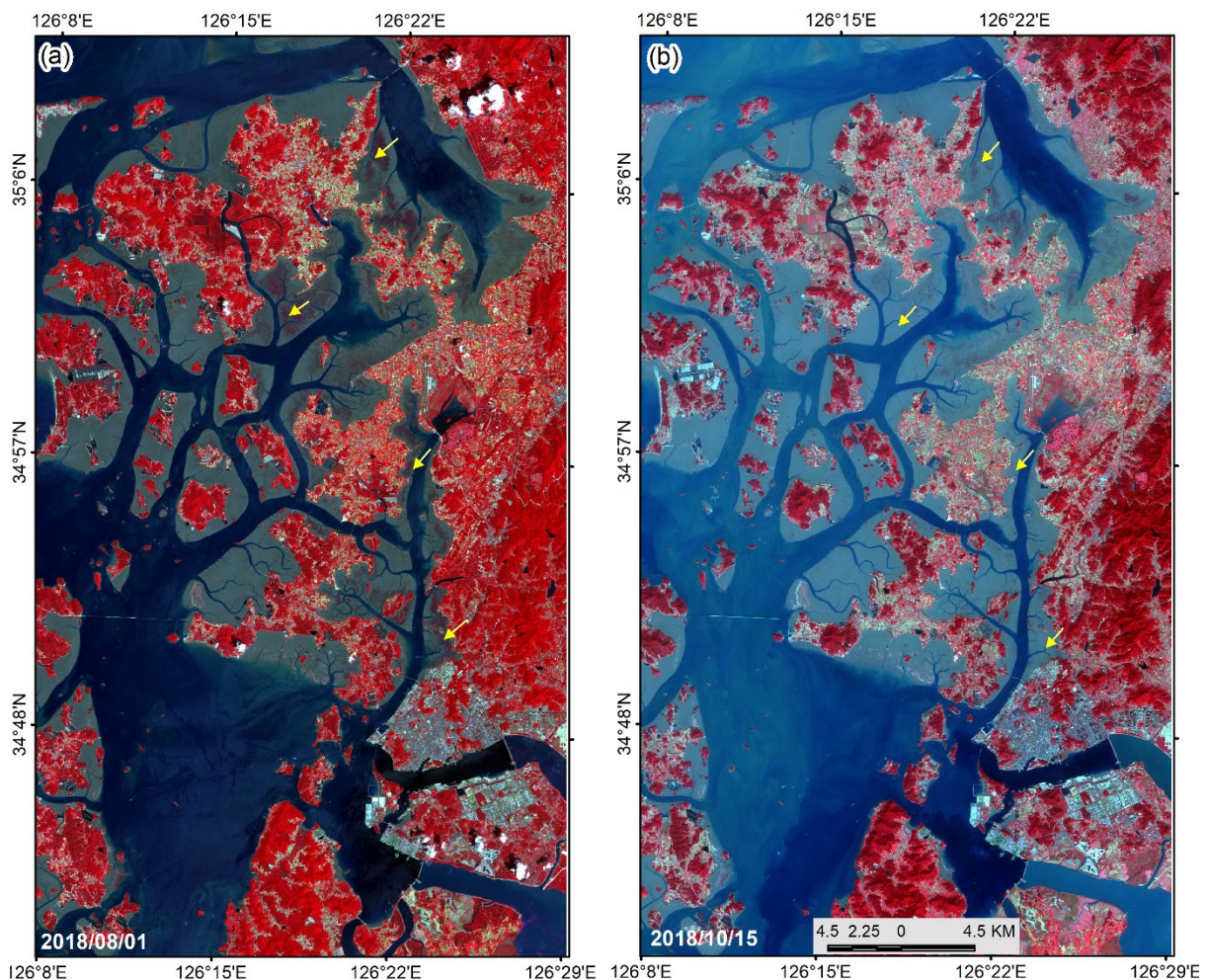
178 **3. Data and Methods**

179 **3.1 Data Sources and pre-processing**

180 Typhoon-induced coastal dynamics along the Mokpo coast have been studied using the
181 pre-and post-event Sentinel-2 MSI images. A multispectral instrument (MSI), Sentinel-2,
182 consists of two polar-orbiting satellites, Sentinel-2A and Sentinel-2B, launched in June 2015
183 and March 2017, respectively (ESA, 2020). The Sentinel 2 MSI has a 290 km wide field of

184 view, a minimum revisits period of five days, 13 spectral bands ranging from visible to
185 shortwave infrared (SWIR), and spatial resolution of 10m (4 bands), 20m (6 bands), & 60m (3
186 bands) (ESA, 2020). The Sentinel-2 User Manual describes the MSI's radiometric, spectral,
187 and spatial characteristics (ESA, 2020).

188 The cloud-free Sentinel-2 MSI level 1C satellite images with a relatively fine spatial
189 resolution (10m) for the pre-and post-typhoon period have been downloaded from the
190 Copernicus Scientific Data Hub (<https://scihub.copernicus.eu/dhus/>) as depicted in Figure 2.
191 Level 1C is a 12-bit radiometric product that was presented the top of the atmospheric
192 reflectance value (Phiri et al., 2021). The open-source software SNAP (Sentinel Application
193 Platform) has been used to process the Sentinel-2 MSI images such as masking, band
194 visualization, atmospheric correction etc. We used SANP's iCOR tool (image correction for
195 atmospheric effect) for atmospheric correction of the Sentinel 2 MSI data over the land and
196 water (Tian et al., 2020; Keukelaere et al., 2018). After that, satellite remote sensing reflectance
197 (R_r) images were used to monitor short and medium-term coastal dynamics in the Mokpo
198 coastal region.



199

200 Figure 2: Pre (a) and post-typhoon (b) standard false color composite of reflectance image of
 201 the Mokpo coastal region (Sentinel-2 MSI level 1C satellite images are downloaded
 202 from <https://scihub.copernicus.eu/dhus/>). The arrows indicate extensive vegetation
 203 damage due to typhoon Soulik.
 204

205 On the other hand, to exclude the impact of tidal changes, satellite images have been
 206 chosen during low tide conditions (Maiti and Bhattacharya, 2009). The tide height has been
 207 computed using the WXTide32 program (Hopper, 2004). Several researchers have discussed
 208 the significance of low tide satellite data for coastal mapping and dynamics modeling (Nayak,
 209 2002). The details of pre- and post-typhoon satellite data used in the study are listed in Table
 210 1. In addition, the coastal morphology was also investigated using high-resolution (5m×5m)
 211 topography data (i.e., LiDAR DEM) provided by the Korean National Geographic Information
 212 Institute (NGII) and bathymetry data obtained from GMRT (<https://www.gmrt.org>) (Fig. 1b).

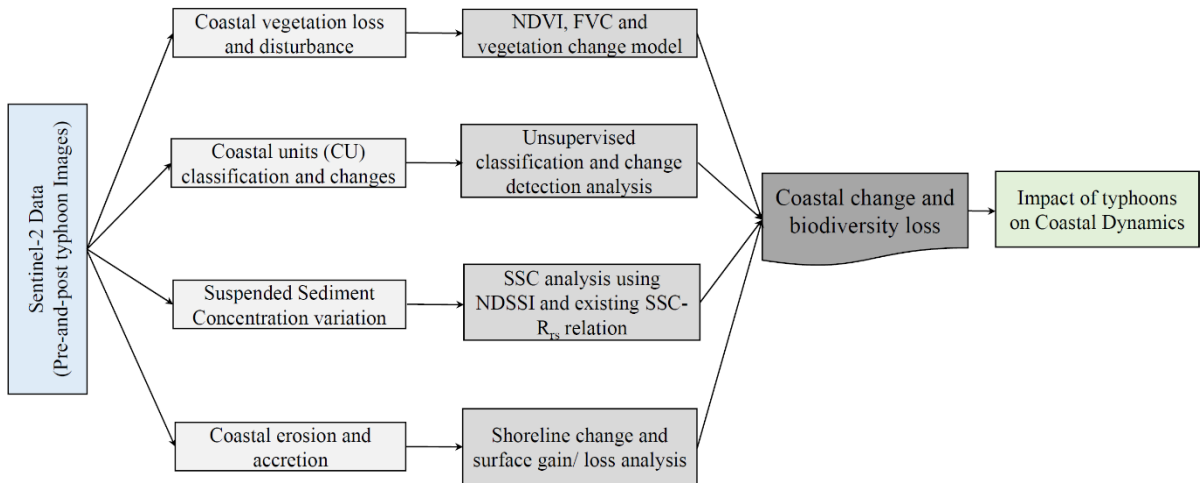
213 Table 1. The details of Sentinel-2 MSI data used for coastal dynamic modeling.

Periods	Date of acquisition	Sensor	Cloud cover (%)	Tidal Height (m)
Pre-typhoon	2018/08/01	Sentinel-2B MSI	1.3464	0.77
Post-typhoon	2018/10/15	Sentinel-2B MSI	0.6548	1.01
	2019/10/20	Sentinel-2B MSI	2.8444	1.02

214

215 3.2. Typhoon-induced coastal dynamic modeling

216 The present study addresses the typhoon Soulik-induced morphodynamics over the
 217 Mokpo coast region, specifically examining short and medium-term coastal changes. Short-
 218 term coastal erosion refers to the rapid erosion processes and coastal alterations that occur
 219 immediately after typhoons or over short durations, typically within days, weeks, or months.
 220 Contrarily, medium-term coastal change refers to erosion processes and coastal changes that
 221 take place over a period of time ranging from a few months to a few years. It involves the
 222 restoration and stabilization of coastal land surfaces after the typhoon. Figure 3 depicts an
 223 integrated flowchart of the impact of a typhoon on a coastal system. The outline of the study is
 224 divided into four sections: (a) coastal vegetation disturbance mapping, (b) coastal landform
 225 mapping and change analysis, (c) suspended sediment concentration variation modeling, and
 226 (d) coastal erosion and accretion analysis. The details methodology of each objective has been
 227 discussed in the subsequent section.



228

229 Figure 3. Geospatial-based approach for typhoon-induced coastal dynamics analysis.

230 3.2.1 Analyses of coastal vegetation loss and disturbance

231 Vegetation damage severity mapping (VDSM) has been performed using pre-and post-
 232 event satellite images. NDVI and FVC are widely used techniques for measuring vegetation
 233 density, health status, regional vegetation condition, and detecting vegetation disturbances (Xu
 234 et al., 2021; Mishra et al., 2021b; Wang et al., 2010; Yang et al., 2018, Wang and Xu, 2018;
 235 Carlson and Ripley, 1997). Subsequently, numerous studies (Xu et al., 2021; Mishra et al.,
 236 2021a; Charrua et al., 2021; Shamsuzzoha et al., 2021; Kumar et al., 2021; Nandi et al., 2020;
 237 Wang and Xu, 2018; Konda et al., 2018; Zhang et al., 2013; Rodgers et al., 2009) have shown
 238 that the NDVI and FVC is a reliable indicator of post-typhoon damage detection. Therefore, in
 239 this study, the vegetation damage due to typhoon Soulik has been determined using the NDVI
 240 and FVC approach. The NDVI has been calculated by using the following Eq. (1) (Rouse et
 241 al., 1974; Filgueiras et al., 2019):

$$242 \quad NDVI = \frac{\rho_{NIR} - \rho_{RED}}{\rho_{NIR} + \rho_{RED}} \quad (1)$$

243 where ρ_{NIR} and ρ_{RED} are the spectral reflectances corresponding to the eighth (832.8–
 244 832.9nm) and fourth (664.6– 664.9nm) Sentinel-2 MSI bands, respectively (Xu et al., 2021).
 245 In general, NDVI values range from -1.0 to 1.0; the higher the NDVI value, the better the
 246 conditions for vegetation development, and extremely low values indicate the presence of
 247 water. Furthermore, the NDVI value above 0.4 indicates vegetated surfaces, and those between
 248 0.25 and 0.40 signify soils with the presence of vegetation (Charrua et al., 2021). The vigor of
 249 the vegetation increases as the NDVI values come closer to 1.00 (Rouse et al., 1974). Numerous
 250 studies have established the NDVI threshold for vegetated land (e.g., Xu et al., 2021; Wong et

251 al., 2019; Liu et al., 2015; Eastman et al., 2013; Yang et al., 2012; Sobrino et al., 2004). Most
252 researchers noted that the NDVI threshold value for vegetation cover typically ranges from
253 0.15-2.0 (Xu et al., 2021; Eastman et al., 2013; Sobrino et al., 2004). Therefore, the vegetated
254 pixels (e.g., NDVI threshold > 0.20) present in pre and post-typhoon NDVI images have been
255 used for vegetation severity analysis. The NDVI threshold is considered to reduce the effect of
256 land cover change from the pre-typhoon (2018-08-01) to post-typhoon (2018-10-15) periods.

257 The degree of vegetation damage has been determined by comparing the NDVI values
258 of the pre-and post-typhoon periods. Various researchers have frequently used the direct
259 difference of NDVI to determine the damage severity caused by typhoons to naturally
260 vegetated land (Wang and Xu, 2018; Konda et al., 2018). It has been calculated on a cell-by-
261 cell basis by subtracting the pre-typhoon NDVI image from that of the post-typhoon in ArcGIS
262 software using map algebra (Zhang et al., 2013; Cakir et al., 2006). The following equation is
263 used to calculate the $\Delta NDVI$ (Wang and Xu, 2018),

$$264 \quad \Delta NDVI = NDVI_{post-typhoon} - NDVI_{pre-typhoon} \quad (2)$$

265 The difference in NDVI (i.e., $\Delta NDVI$) illustrates the change in natural vegetation, while a
266 negative $\Delta NDVI$ value indicates the damage inflicted by a typhoon to the vegetation cover (Xu
267 et al., 2021).

268 The relative change in NDVI value has been used to investigate the geo-ecological
269 impact on the forest area (Mishra et al., 2021b). The relative vegetation changes ($NDVI_r$) after
270 Soulik have been determined by using the following Eq. (3) (Kumar et al., 2021),

$$271 \quad NDVI_r = \frac{\Delta NDVI}{NDVI_{pre-typhoon}} \times 100 \quad (3)$$

272 where the negative $NDVI_r$ value indicates vegetation loss caused by typhoons, and the positive
273 $NDVI_r$ value shows vegetation gain. The $NDVI_r$ value has been classified into three categories
274 corresponding to pixels with decreased, no change, or increased vegetation cover.

275 On the other hand, we analyze FVC in conjunction with NDVI, which provide
276 additional insights into vegetation conditions and damage severity. Numerous researchers
277 (Wang and Xu, 2018; Song et al., 2017; Bao et al., 2017; Chu et al., 2016; Amiri et al., 2009)
278 used FVC to analyze vegetation damage, restoration, recovery, and inter-annual variability. In
279 the present study, FVC was calculated before and after the typhoon using the derived NDVI
280 data (Wang and Xu, 2018). It is expressed as a percentage and can range from 0 to 100%. The
281 formula of FVC is as follows (Wang and Xu, 2018; Amiri et al., 2009; Carlson and Ripley,

282 1997),

$$283 \quad FVC = [(NDVI - NDVI_m)/(NDVI_{max} - NDVI_m)]^2 \quad (4)$$

284 where, $NDVI_m$ and $NDVI_{max}$ represent the $NDVI_{min}$ and $NDVI_{max}$ values calculated using
285 equation (1) (Zhang et al., 2021; Ge et al., 2018). The calculated FVC values vary between 0
286 and 1. After that, the FVC values were converted to percentages to fit the actual FVC
287 classification scheme (Wang and Xu, 2018), which consists of five classes: high (80-100%),
288 medium-high (60-80%), medium (40-60%), medium-low (20-40%), and low (0-20%). Further,
289 the difference in FVC values between the pre-and post-typhoon images was used to calculate
290 the extent of vegetation damage using the following equation,

$$291 \quad \Delta FVC = FVC_{post-typhoon} - FVC_{pre-typhoon} \quad (5)$$

292 where, ΔFVC denotes the difference between the pre and post-typhoon FVC. The ΔFVC value
293 represents alterations in vegetation conditions and damage intensity, while a negative value of
294 ΔFVC indicates the extent of damage caused by a typhoon to vegetation cover (Wang and Xu,
295 2018).

296

297 **3.2.2 Coastal landform classification and change analysis**

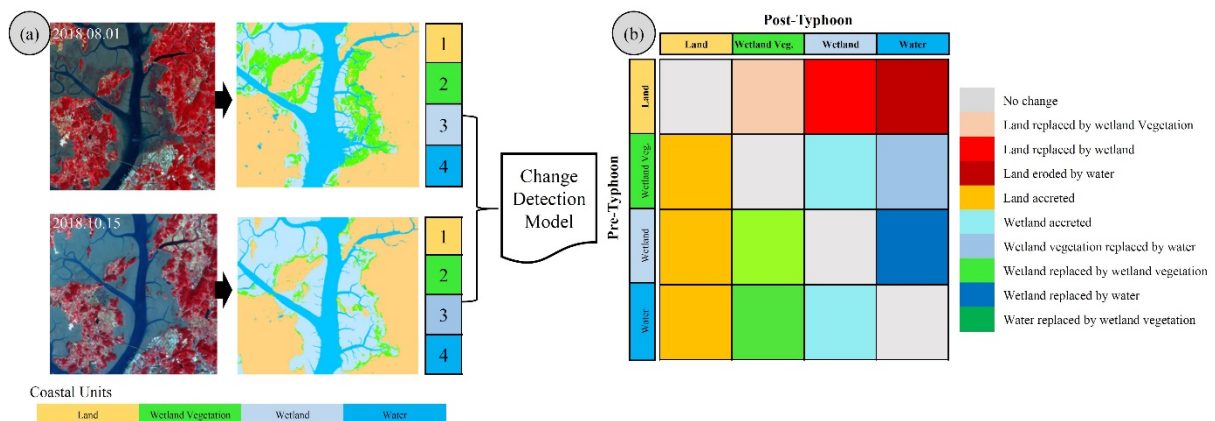
298 Typhoons have adversely affected the coastal landform and ecology of the south and
299 west coasts of the Korean peninsula every year. Therefore, a GIS-based coastal change model
300 has been developed to understand the morphodynamics of coastal landforms during typhoons.
301 In the present study, we considered four coastal landform classes, i.e., wetland, wetland
302 vegetation, land, and water, for the coastal morphodynamic analysis (Maiti and Bhattacharya,
303 2011). The method consists of two algorithms, i.e., (a) the ISODATA algorithm used to classify
304 the coastal landform with four main classes, i.e., water, wetland, wetland vegetation, and land,
305 and (b) the change detection technique used to quantify the short-term and medium-term
306 coastal changes. In this approach, we accentuate in-depth morphological changes and
307 emphasize minor changes along the Mokpo coast caused by typhoon Soulik.

308 The pre-and post-typhoon Sentinel-MSI images have been classified using the
309 unsupervised classification technique to distinguish among different coastal landforms of the
310 study region. This approach is used to determine which types of coastal landforms were
311 adversely affected by Typhoon Soulik and which of them have recovered more quickly than
312 others. ERDAS Image software has been used to run the unsupervised classification algorithm
313 (ERDAS, 1997). Based on the k-means algorithm, this technique reduces variability within
314 pixel clusters (Charrua et al., 2021; Aswatha et al., 2020; Bhowmik et al., 2013). Finally, pre-

315 and post-typhoon Sentinel-2 MSI images have been classified into four coastal landform
 316 classes: land, water, wetland, and wetland vegetation.

317 The accuracy assessment is a commonly used method to determine how closely the
 318 classified map matches the reference data (Congalton, 1991). In the present study, the classified
 319 data (i.e., coastal landforms maps) have been derived through an unsupervised classification
 320 technique, while 550 random samples collected from different parts of the Sentinel- 2MSI
 321 standard false-color image are considered reference data. Thereafter, a confusion matrix was
 322 developed based on the reference and classified data to evaluate accuracy statistics (Story and
 323 Congalton, 1986). The *kappa* coefficient (*k*) has been used to determine the quantitative
 324 accuracy of the classified map (Landis and Koch, 1977). The assessment is quantified using
 325 three different statistics: overall accuracy, producer accuracy, and user accuracy (Story and
 326 Congalton, 1986). The model's precision is classified into five categories based on the *k* values:
 327 near perfect ($k > 0.8$), substantial ($0.6 < k < 0.8$), moderate ($0.4 < k < 0.6$), fire ($0.2 < k < 0.4$),
 328 and poor ($k < 0.2$) (Landis and Koch, 1977).

329 The land transformation model based on mutual spatial replacements has been applied
 330 during the post-classification stage, as shown in Figure 4. The classified coastal landform
 331 classes, such as land, wetland, wetland vegetation, and water, have been spatially replaced in
 332 order to create coastal-change units. For example, the coastal landform class of wetland
 333 vegetation in the pre-typhoon period replaced by water in the post-typhoon period indicates the
 334 change class of wetland vegetation replaced by water. A total of nine coastal-change classes
 335 have been derived, as illustrated in Figure 4(b).



337 Figure 4. The coastal-change model exhibits spatial replacements among coastal landform
 338 classes.

340 **3.2.3 Suspended sediment concentration modeling**

341 The suspended sediment concentration (SSC) distribution in coastal regions is a
342 significant indicator of changes in the marine environment caused by typhoon-induced storm
343 surges, strong waves, and subsequent coastal flooding (Min et al., 2012; Gong and Shen, 2009).
344 In a short period, a typhoon may drastically influence the water column structures (Souza et
345 al., 2001), change the transport and deposition of sediment (Li et al., 2015), and affect the
346 distribution of nutrients and biological production in the affected seas (Wang et al., 2016).
347 Extreme storms or typhoons can modify suspended sediment distribution in coastal areas,
348 which can significantly change marine habitats (Chau et al., 2021; Lu et al., 2018; Li and Li,
349 2016). Due to strong typhoon wind stress, the concentration of suspended particles in the
350 seawater column and sediment resuspension may increase dozens of times before and after the
351 event (Lu et al., 2018; Bian et al., 2017). Thus, typhoons significantly affect suspended
352 sediment movement in the coastal region (Zhang et al., 2022; Li and Li, 2016; Goff et al.,
353 2010). The spatiotemporal distribution of SSC can be impacted by variations in tidal phase,
354 runoff, and wind speed (Tang et al., 2021). Furthermore, the resuspension of sediment can
355 cause numerous problems in ocean engineering and change the region's ecology (Kim, 2010).
356 The amount of material delivered to and advected across the shelf by typhoons is considerably
357 larger than that of winter storm systems (Dail et al., 2007). The southern and western part of
358 the Korean peninsula is affected by an average of three typhoons annually passing through the
359 Yellow Sea (KMA, 2018; Altman et al., 2013). Some studies on SSC distribution impacted by
360 artificial construction along the coastal region of the Yellow Sea have been undertaken by
361 several researchers (i.e., Lee et al., 2020; Eom et al., 2017; Min et al., 2012, 2014; Choi et al.,
362 2014). However, the effects of typhoons on the sedimentary environment in the Mokpo coastal
363 region have not yet been investigated. Therefore, it is imperative to carry out regional-scale
364 SSC mapping and coastal modifications to reveal changes in the marine environment and
365 sediment transport mechanisms over the typhoon period.

366 Remote sensing has long contributed to the advancement of water quality studies
367 (Hossain et al., 2021). In the present study, we attempted to calculate both the qualitative and
368 quantitative SSC in the inner-shelf region of the Mokpo coast using Sentinel-2B MSI data. The
369 relative suspended sediment concentration has been calculated from pre- and post-typhoon
370 Sentinel-2B MSI images using the NDSSI. NDSSI has been used in various water quality
371 research (Kavan et al., 2022; Hossain et al., 2010). Further, many studies (Shahzad et al., 2018;
372 Arisanty & Saputra, 2017) have successfully used Landsat and Sentinel-2 data to calculate

373 NDSSI. This index determines the relative concentration of suspended sediment, with values
 374 ranging from -1 to 1, where -1 indicates the highest concentration and +1 indicates the lowest
 375 (Hossain et al. 2010). The NDSSI has been calculated by using Eq. (6).

$$376 \quad NDSSI = \frac{\rho_{Blue} - \rho_{NIR}}{\rho_{Blue} + \rho_{NIR}} \quad (6)$$

377 where ρ_{Blue} and ρ_{NIR} represent the surface reflectances of Band 2 (492.1– 492.4 nm) and
 378 Band 8 (832.8 – 833.0 nm) of Sentinel-2 MSI data, respectively. The NDSSI is based on the
 379 observation that turbid waters reflect more in the NIR band but less in the visible band. The
 380 negative NDSSI value represents that the reflectance of water in the NIR band is greater than
 381 that in the blue band (Shahzad et al., 2018; Hossain et al., 2010). Therefore, the positive values
 382 of NDSSI represent lower SSC or more transparent water, while a negative value indicates
 383 higher SSC. The spatial patterns of relative SSC during the typhoon period have been
 384 determined using the NDSSI.

385 On the other hand, the empirical model has also been used to quantify the suspended
 386 sediment concentration before and after typhoon Soulik. This method is widely used for SSC
 387 mapping and monitoring around the world (Eom et al., 2017; Hwang et al., 2016; Son et al.,
 388 2014; Min et al., 2012; Lee et al., 2011; Choi et al., 2014). For this purpose, we reviewed the
 389 existing relations between the in-situ SSC (SSC, g/m³) and remote sensing reflectance (R_r)
 390 developed by various researchers for the southern and western coasts of South Korea, as
 391 illustrated in Table 2. In the present study, the SSC algorithm developed by Choi et al. (2014)
 392 for the Mokpo coastal region based on the in-situ SSC and a spectral ratio of water reflectance
 393 around 660nm has been used to quantify the SSC distribution. The atmospheric corrected
 394 sentinel-2 MSI image (Red band) has been used to calculate the SSC.

395

396 Table 2. Relationship between the remote sensing reflectance (R_r) and suspended sediment
 397 concentration (SSC, g/m³).

Authors	Relation	Region	Wavelength (nm)
Min et al. (2012) Min et al. (2006)	$Y=0.24e^{188.3x}$	Saemangeum coastal area	560nm
Choi et al. (2014)	$Y=1.545e^{179.53x}$	Mokpo coastal area, Gyeonggi Bay	660nm
Lee et al. (2011)	$Y=16.2064e^{15.3529x}$	Gwangyang Bay and Yeosu Bay	565nm
Choi et al. (2012) Lee et al. (2020)	$Y=1.7532e^{204.26x}$	Yellow Sea	660nm
Eom et al. (2017)	$Y=1.5119e^{179.85x}$	Nakdong River	660nm

Min et al. (2004)	$Y=0.99e^{199.9x}$	Saemangeum	560nm
-------------------	--------------------	------------	-------

398

399 3.2.4 Coastal erosion and accretion analysis

400 The shorelines (i.e., land and water boundary) of the Mopko coast for short and medium
 401 periods have been extracted using a semi-automatic technique (Maiti and Bhattacharya, 2009).
 402 Here, we used the normalized difference water index (NDWI) and manual digitization
 403 approach to separate the land and water boundary. The technique is widely used for dividing
 404 land and water boundary (Santos et al., 2021; Dai et al., 2019). By using Sentinel-2 imagery,
 405 NDWI can be achieved with the following formula (McFeeters, 1996),

$$406 \quad NDWI = \frac{\rho_{Green} - \rho_{NIR}}{\rho_{Green} + \rho_{NIR}} \quad (7)$$

407 where ρ_{Green} is the green band, and ρ_{NIR} is the near-infrared band of Sentinel-2 MSI data.

408 The extracted land and water boundary of the Mokpo region are then converted into
 409 polygons, and the shoreline has been determined using ArcGIS software. The shoreline change
 410 statistics have been calculated using the DSAS program (Thieler et al., 2009). The extracted
 411 shoreline for pre-and post-typhoon periods has been merged, and a 10m interval transect
 412 perpendicular to a baseline has been created (Santos et al., 2021). After that, the NSM method
 413 was used to calculate the total shoreline movement (in meters) between the pre-and post-
 414 typhoon shoreline positions of each transect (Kermani et al., 2016).

$$415 \quad NSM = sh_{post} - sh_{pre} \quad (8)$$

416 where sh_{post} and sh_{pre} represent the post and pre-typhoon shoreline positions, respectively.

417 On the other hand, the back-shore surface area changes due to shoreline movement
 418 (retreat/advance) over the typhoon period has also been calculated using the geo-statistical
 419 analyst tool. Several researchers (Awad and El-Sayed, 2021; Deabes, 2017; Karmani et al.,
 420 2016) have also previously mapped the surface changes of the backshore region. To create the
 421 surface area-change map, we first generated two polygon layers based on the extracted
 422 shoreline, one for the pre-and one for the post-typhoon periods. Next, we utilized the
 423 Symmetrical Difference tool in ArcGIS software to compute the difference between these
 424 polygon layers during the period affected by the typhoon. Finally, two feature classes have
 425 been derived, one for erosion and another for accretion. In addition, the attribute table contained
 426 in each zone illustrates the magnitude of spatial changes (amounts of erosion and accretion)
 427 during the typhoon period.

428

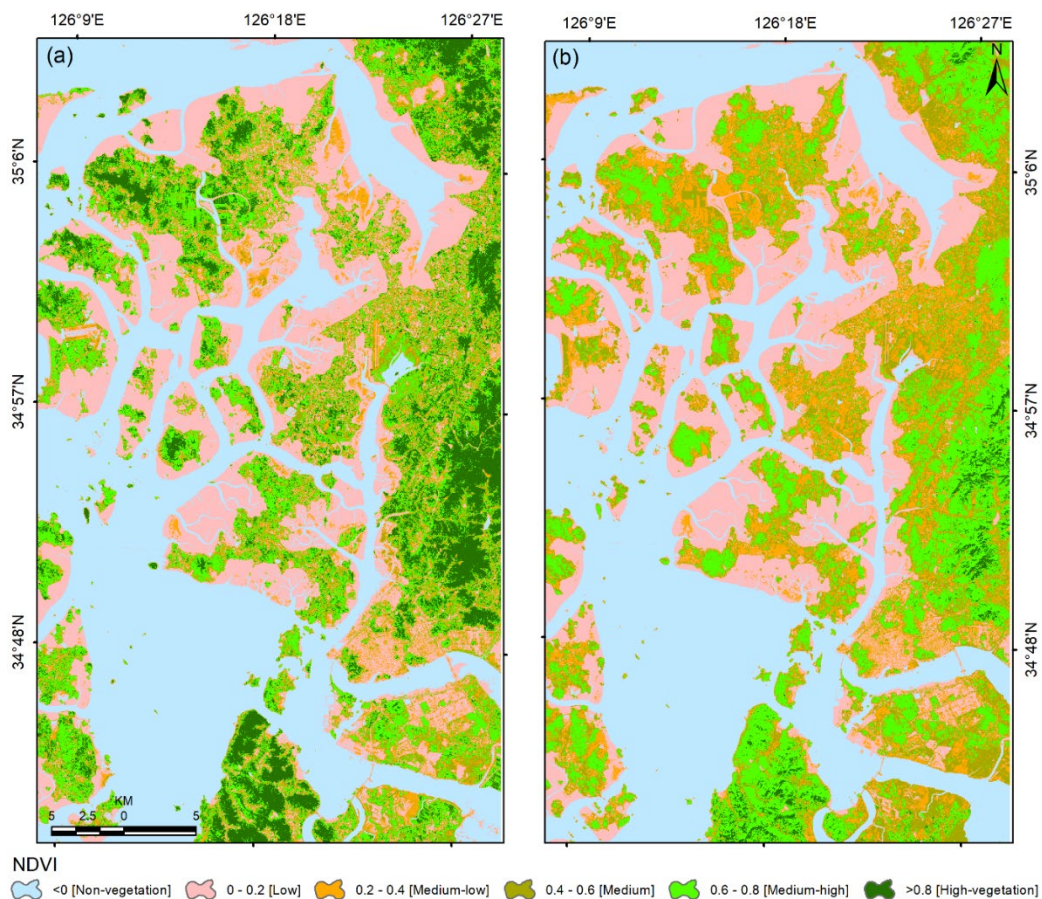
429 4. Result and Discussion

430 **4.1 Vegetation damage severity mapping (VDSM) before and after Typhoon**

431 *4.1.1 VDSM based on the NDVI and FVC analysis*

432 The VDSM shows the degree of vegetation damage due to typhoons. The comparison
433 of pre-and post-typhoon NDVI and FVC distribution shows a significant loss of vegetated land
434 as the number of no-productivity and low-productivity pixels increases in the post-typhoon
435 NDVI and FVC image.

436 Figure 5 depicts the spatial distribution of pre and post-typhoon NDVI images. Further,
437 to determine the severity of vegetation damage, the pre-and post-typhoon NDVI image has
438 been classified into six categories, namely non-vegetation (-1.0-0.0), low-vegetation (0.0-0.2),
439 medium-low vegetation (0.2-0.4), medium vegetation (0.4-0.6), medium-high vegetation (0.6-
440 0.8) and high vegetation (0.8-1.0). The pre and post-typhoon mean NDVI values were observed
441 to be 0.159 and 0.143, respectively, indicating a mean NDVI value decline of 0.016 after the
442 typhoon.



443
444 Figure 5. Status of vegetation greenness based on the NDVI data for the (a) pre-Soulik (01st
445 August 2018) and post-Soulik (15th October 2018) period.
446

447 Table 3 depicts the area changes for each NDVI category over the typhoon period. It

448 has been observed that the high NDVI values (>0.8) have changed drastically after typhoon-
 449 Soulik. The area changes in the low and non-vegetation categories along the Mokpo coastal
 450 region revealed that the wetland (mudflat) had accreted after the typhoon. On the other hand,
 451 the post-typhoon image was acquired two months after typhoon Soulik, which suggests that
 452 the grasses and crops have recovered well. This recovery is reflected in Table 3 from medium-
 453 low to medium-high NDVI levels.

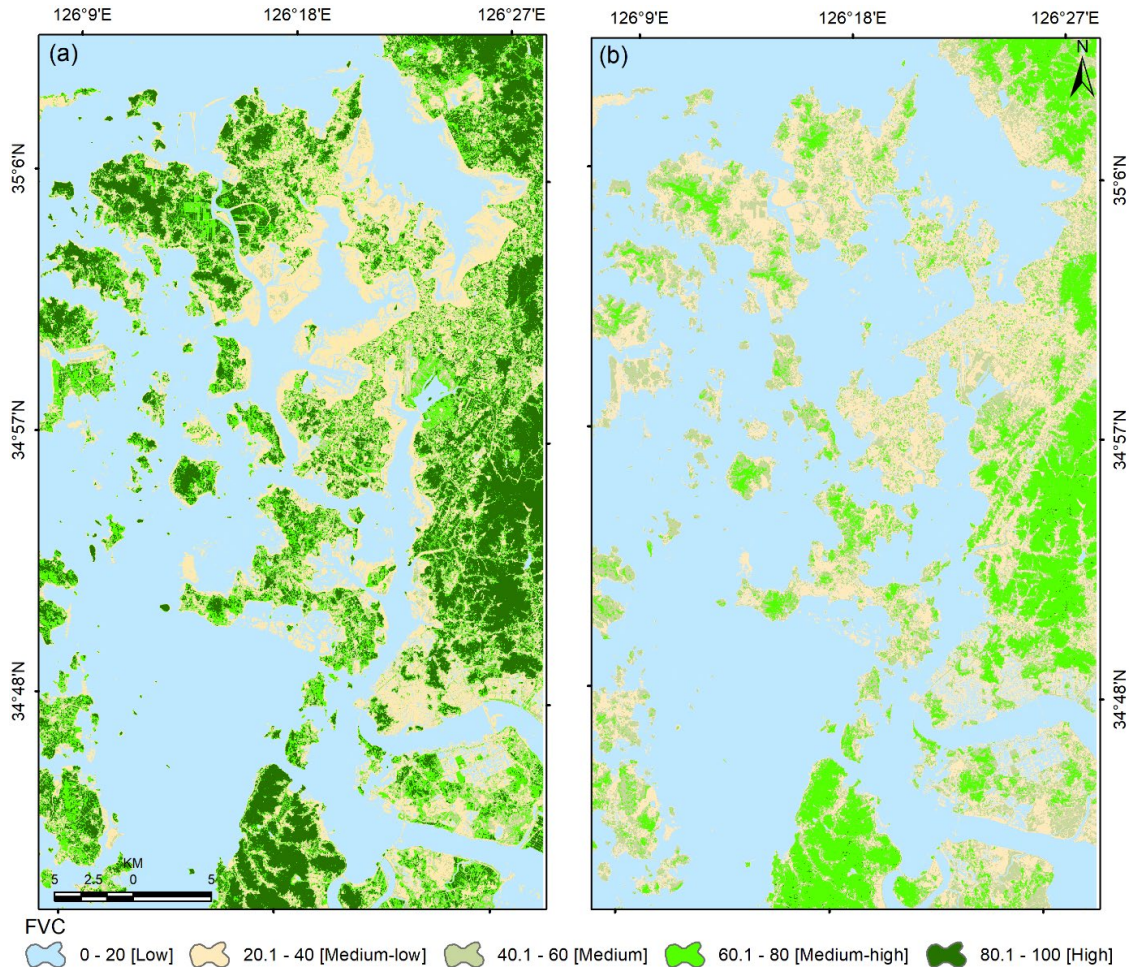
454

455 Table 3. NDVI distribution over the study area before and after the typhoon.

NDVI levels	Pre-typhoon (km ²)	Post-typhoon (km ²)	Change (km ²)
Non-vegetation (-1 to 0)	673.7	647.6	-26.2
Low (0 to 0.2)	430.4	415.2	-15.2
Medium-low (0.2 to 0.4)	141.6	243.3	101.6
Medium (0.4 to 0.6)	132.5	225.3	92.8
Medium-high (0.6 to 0.8)	283.7	294.4	10.7
High (0.8 to 1.0)	183.6	19.8	-163.8

456

457 On the other hand, the physical presence of vegetation has also been measured using
 458 FVC analysis. In general, NDVI provides information on the health and productivity of
 459 vegetation, while FVC provides information on the physical presence and distribution of
 460 vegetation. Figure 6 depicts the pre- and post-typhoon FVC map of the Mopko coast. The area
 461 of each FVC category is illustrated in Table 4. The results reveal that the typhoon caused a
 462 substantial decrease in FVC in the area, with the average FVC reducing significantly from
 463 33.43% to 23.64% after the typhoon. It was observed that the medium-high to high FVC area
 464 decreased from 485.4 km² to 211.9 km², while the medium-to-low FVC area increased from
 465 1359.8 km² to 1633.3 km². The high FVC vegetation category was more severely affected and
 466 decreased considerably after the typhoon. These results indicate that the typhoon significantly
 467 impacted the wetland vegetation in the region.



468

469

470

471

Figure 6. Status of vegetation based on the FVC analysis for the (a) pre-Soulik (01st August 2018) and post-Soulik (15th October 2018) period.

472

Table 4. Summary of FVC classes before and after the typhoon.

FVC levels (%)	Pre-typhoon (km ²)	Post-typhoon (km ²)	Change (km ²)
Non-vegetation (<20)	890.3	1053.3	162.943
Medium-low (20-40)	327.4	319.6	-7.811
Medium (40-60)	142.4	260.6	118.205
Medium-high (60-80)	206.1	211.5	5.365
High (80-100)	279.4	0.7	-278.671

473

474

475

476

477

478

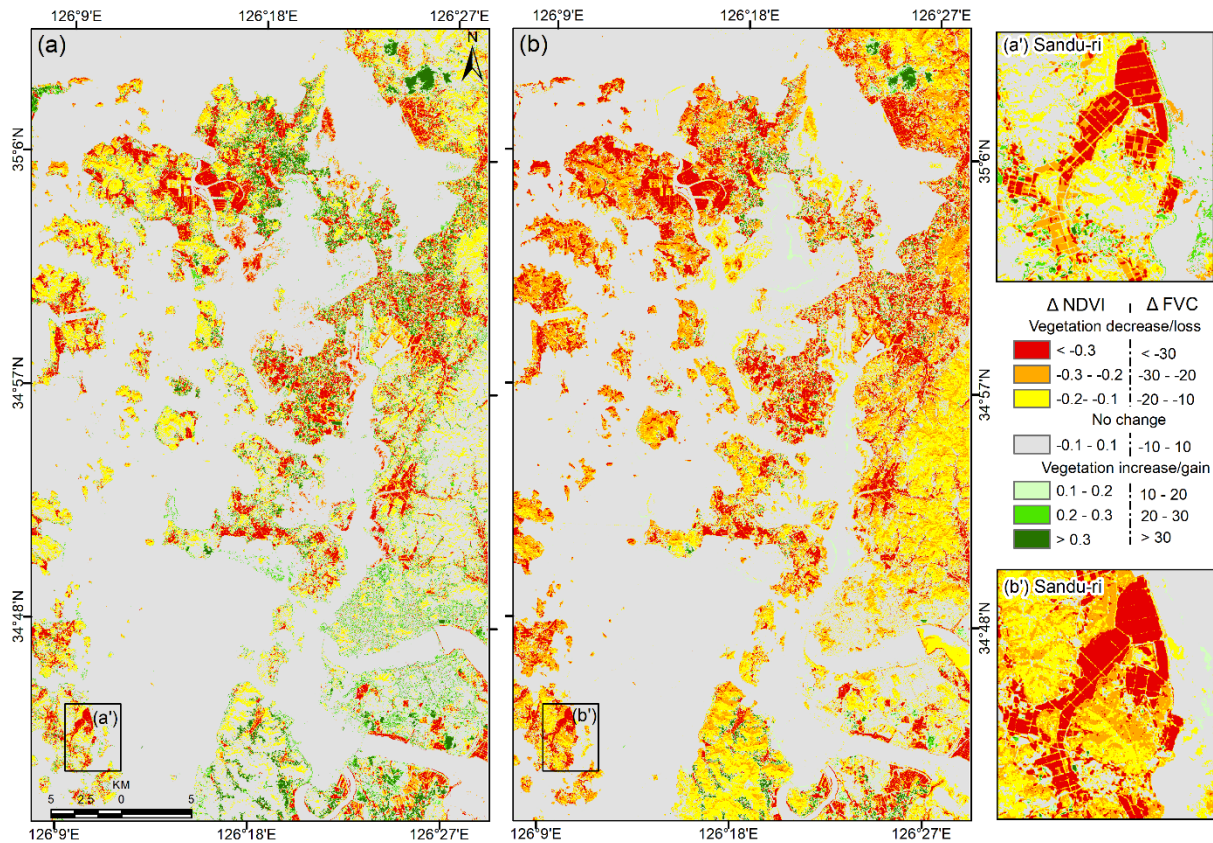
479

In order to determine the damaged vegetation areas along the Mokpo coast, we compared pre-and post-typhoon NDVI images. A decrease in Δ NDVI is one of the most distinctive features of abrupt canopy modifications detectable by optical remote sensing (Xu et al., 2021). Thus, we can only determine vegetation deterioration from the two NDVI images. Subsequently, an NDVI threshold of 0.2 has been used to extract only vegetation features from the pre-and post-typhoon NDVI images. The threshold value has been manually adjusted to

480 achieve the highest accuracy of vegetation pixels. The extracted vegetated pixels have been
481 compared with reference samples randomly collected from the original high spatial resolution
482 images to determine the accuracy (Schneider, 2012; Xu et al., 2021). The two extracted
483 vegetation images obtained within six or seven weeks of typhoon Soulik's (i.e., before the
484 damaged vegetation had recovered) exhibits an overall accuracy of 95.7 % for pre-typhoon and
485 94.5% for the post-typhoon period.

486 Figure 7(a) depicts the spatial distribution of Δ NDVI, where the highest Δ NDVI
487 indicates a region with highly impacted vegetation areas. The negative Δ NDVI is attributed to
488 about 26.7% of the total area (1845.60 km²), which suggests that Typhoon Soulik affected
489 approximately 493.98 km² of vegetated land. The lowest Δ NDVI value is -0.89, which
490 indicates either tree wind throws or a change in land surface cover from vegetation to build-up
491 land or other non-vegetation covers (Zhang et al., 2013). The results showed that wetland
492 vegetation and agricultural land experienced the most significant NDVI changes, with Δ NDVI
493 values below -0.3. This suggests that these two types of land cover were severely affected by
494 typhoon Soulik.

495 On the other hand, Figure 7(b) displays the change map obtained from the difference in
496 FVC (Δ FVC), which reveals areas of altered vegetation after the typhoon. The negative Δ FVC
497 is attributed to about 32.07% of the total area, which suggests that Typhoon Soulik affected
498 approximately 591.89 km² of vegetated land. It has also been observed that the pure vegetation
499 pixels (i.e., NDVI>0.6 and FVC>60%) were drastically changed over the typhoon period. The
500 changed area determined for NDVI and FVC is -153.43 km² and -273.40 km², respectively
501 (Tables 3 & 4). The results obtained from both techniques indicate a significant decrease in
502 vegetation cover after the typhoon. The probable reason for the change is that Typhoon Soulik
503 made landfall close to Mokpo coastal region.



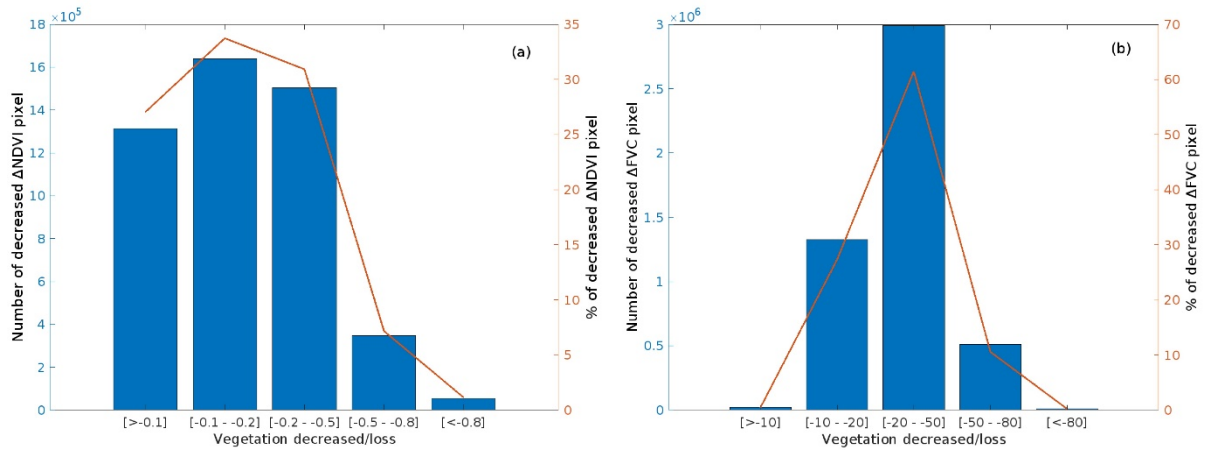
504

505 Figure 7. Vegetation change map of the Mokpo coastal region derived through two different
 506 methods: (a) Δ NDVI and (b) Δ FVC, whereas zoom boxes show the vegetation
 507 damage of Sandu-ri areas.

508

509

Figure 8 compares vegetation damage based on the number and percentage of the
 510 decreased pixel of Δ NDVI and Δ FVC. It exhibits decreased pixels in different categories of
 511 vegetation damage, ranging from low damage to extensive damage. The pixels showing the
 512 most significant vegetation damage (i.e., Δ NDVI -0.2 to -0.5 and Δ FVC -20 to -50%) account
 513 for about 30.9% and 61.5% of the total pixels, respectively. On the other hand, the pixels
 514 showing extensive vegetation damage (i.e., Δ NDVI < -0.5 and Δ FVC < -50%) account for only
 515 8.31% and 10.76% of the total pixels. It was observed that the dominant vegetation in the region
 516 is wetland vegetation, which is mainly due to the prevalence of wetlands or mudflats in the
 517 area. Therefore, the significant vegetation damage implies that wetland vegetation was most
 518 severely impacted during typhoons.

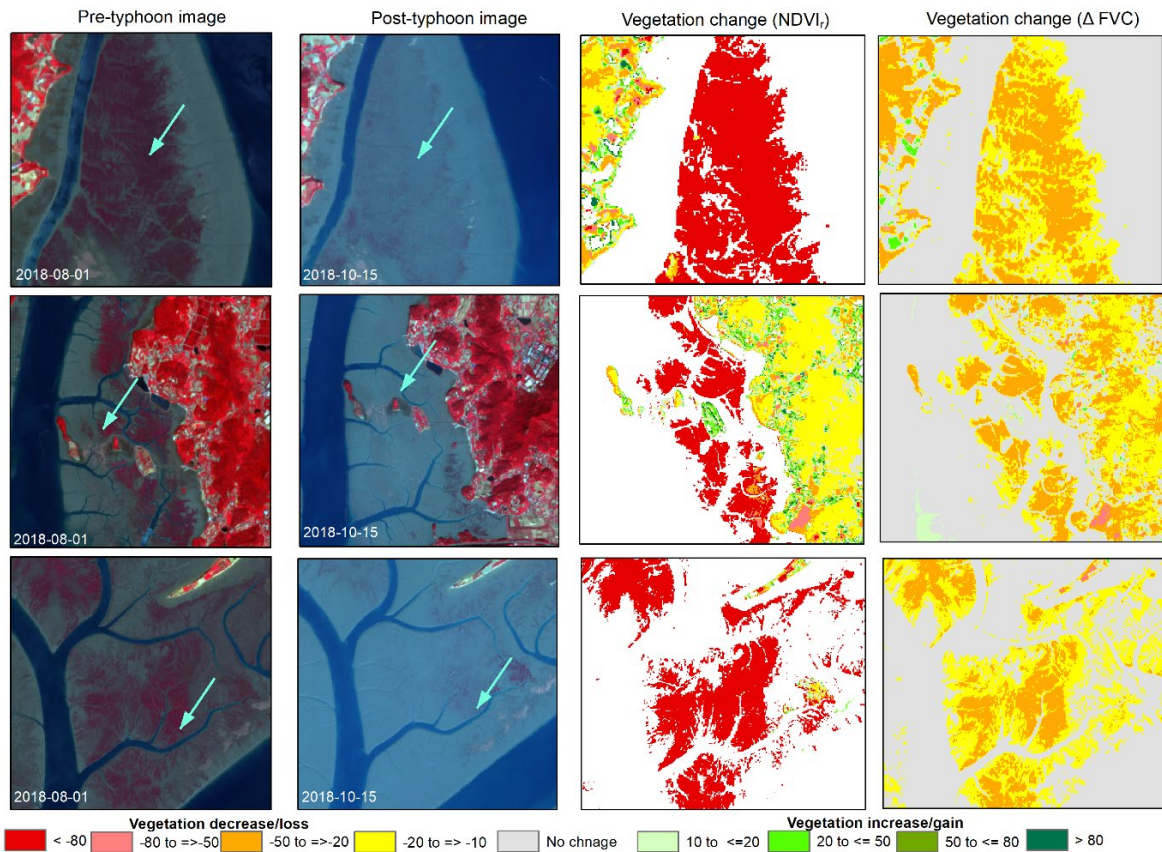


519

520 Figure 8. Comparison of vegetation damaged represented based on the number and percentage
 521 of decreased pixels of (a) $\Delta NDVI$ and (b) ΔFVC .
 522

523 The pre-and post-typhoon Sentinel-2 false-color images and the corresponding relative
 524 change in $NDVI_r$ and ΔFVC values are presented in Figure 9. The standard FCC imagery (left
 525 panel, Fig. 9) for pre and post-typhoon shows that $NDVI_r$ is more effective in detecting areas
 526 of damaged vegetation compared to ΔFVC (right panel, Fig. 9). It was observed that the
 527 typhoon-induced damaged vegetation area (i.e., pixels with $NDVI_r$ and ΔFVC of $<-50\%$)
 528 detected by $NDVI_r$ (106.5 km^2) was greater than that detected by ΔFVC (51.3 km^2). The
 529 dissimilarity in the ability of $NDVI_r$ and ΔFVC to detect the destruction of vegetation caused
 530 by the typhoon can be ascribed to the alteration in the color of the vegetation post-typhoon.
 531 This change can be detected more accurately by $NDVI$ compared to FVC because the
 532 vegetation in the affected areas still existed, and there was not a significant reduction in
 533 vegetation coverage after the event (Wang and Xu, 2018). Thus, $NDVI$ is highly sensitive to
 534 the health status of vegetation and a more appropriate approach for assessing the damage to
 535 vegetation induced by the typhoon, while FVC is more representative of vegetation coverage
 536 status (Wang and Xu, 2018; Jing et al., 2011). Consequently, the dramatic vegetation loss ($<-$
 537 80%) that occurred in mostly wetland vegetation is detected mainly in $NDVI_r$. In addition,
 538 moderate greenness loss has been identified in natural forests. Furthermore, the decrease of
 539 $NDVI_r$ values from higher classes to lower classes indicates that the typhoon has severely
 540 damaged the low-lying coastal regions and the wetland vegetation.

541



542
543
544
545
546
547
548
549

Figure 9. Sentinel-2 MSI standard false color composite images before and after Typhoon Soulik exhibit vegetation damage and the corresponding NDVI_r and ΔFVC (Sentinel-2 MSI level 1C satellite images were downloaded from <https://scihub.copernicus.eu/dhus/>).

4.1.2 Influence of topography on vegetation damage caused by Typhoon Soulik

550
551
552
553
554
555
556
557

The affected area's topography can influence typhoons' impact on vegetation. The interaction between topography and typhoon-generated wind and rain can result in complex and varied patterns of damage across different landscapes (Abbas et al., 2020; Lu et al., 2020; Zhang et al., 2013). This can affect the severity and spatial patterns of vegetation damage. Therefore, the relationship between topography and damaged vegetation has also been established in the present study. For this purpose, high-resolution (5m×5m) DEM data provided by the NGII are used to calculate the region's topographic slope and explore the relationship between topography and typhoon-induced vegetation damage.

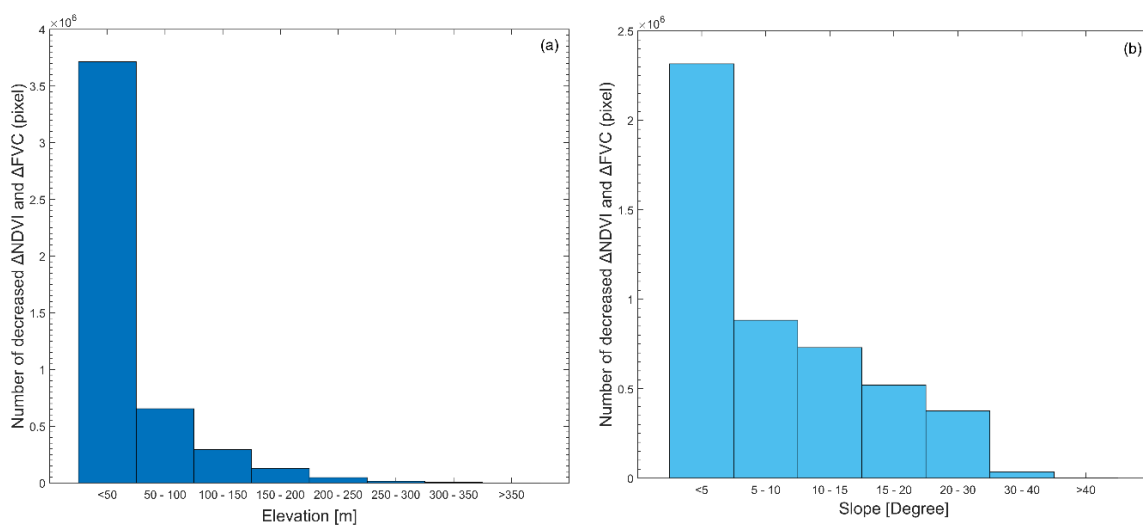
558
559
560
561
562

The Mopko coastal region showed an elevation range between 0 to 403 meters, as shown in Figure 1(b). It was observed that the number of trees damaged by Typhoon Soulik decreased as the elevation increased, as illustrated in Figure 10a. The highest number of damaged trees was observed in areas with an elevation of 50m or lower. This is likely due to the fact that these areas are predominantly covered by wetlands, which can be more vulnerable

563 to strong winds associated with typhoons Soulik. In general, low-lying areas may not have the
 564 same natural windbreaks and barriers as higher elevations, which can exacerbate the impact of
 565 the wind. In addition, low-elevated vegetation may have shallower root systems due to the less
 566 stable soil conditions, making them more vulnerable to uprooting during heavy rainfall or
 567 strong winds (Zhang et al., 2013; Lugo et al., 1983). A significant difference in the number of
 568 decreased Δ NDVI and Δ FVC pixels was observed among different elevation ranges, and a
 569 correlation analysis between the number of damaged pixels and elevations showed a negative
 570 correlation (i.e., damaged pixels decreased with increasing elevation). The majority of
 571 damaged pixels (76.37%) were observed at elevations between 0 and 50m, with a decrease to
 572 13.5% between 51 and 100m. The vegetation exhibited a sharp decline at higher elevations, as
 573 shown in Figure 10(a), with the proportion of pixels displaying negative Δ NDVI and Δ FVC
 574 decreasing to 6.1% between 100 and 150m and decreasing to 0.02% between 350 and 403m.

575 On the other hand, Figure 10(b) illustrates the extent of damaged vegetation across
 576 different slope ranges. It has been noted that there is a negative correlation between the slope
 577 and the percentage of damaged vegetation pixels, indicating that the amount of vegetation
 578 damage decreases with a higher slope. For instance, when the slope was between 0-5°,
 579 approximately 47.63% of vegetation pixels were damaged. As the slope increased, the
 580 percentage of damaged vegetation pixels decreased accordingly, with values of 18.15%,
 581 15.01%, 10.71%, 7.74%, 0.73%, and 0.009% observed for slope ranges of 5-10°, 10-15°, 15-
 582 20°, 20-30°, 30-40°, and greater than 40°, respectively.

583



584

585 Figure 10. The relationship between topography and vegetation damaged due to typhoon
 586 Soulik: (a) numbers of damaged vegetation at different elevation ranges, and (b)
 587 numbers of damaged vegetation at different slope ranges.

588

589 4.2 Coastal morphodynamics over the typhoon period

590 To understand the coastal morphodynamics over the typhoon period (i.e., short-term),
 591 we classified the entire coastal region into four major coastal landform classes: land, wetland
 592 vegetation, wetland, and water (Fig. 11a-b). The accuracy and *kappa* coefficient of the
 593 classified maps exhibited a reasonable degree of consistency with the reference data, as
 594 illustrated in Table 5. The overall accuracy of the pre-and post-typhoon coastal landform maps
 595 was 86.5% and 84.3%, and *kappa* coefficients were 0.82 and 0.79, respectively. The results of
 596 the coastal landform classification showed a reduction in wetland vegetation over the typhoon
 597 period. Table 6 illustrates that before the typhoon, the area of the wetland vegetation class was
 598 4.21% (77.63 km²) of the total area of all categories (1845.60 km²). However, after the hitting
 599 of the typhoon storm, the wetland vegetation area reduced to 1.08% (19.90 km²), recording a
 600 degradation of 57.73 km² (-74.37%).

601

602 Table 5. Accuracy assessment of pre-and post-typhoon classified coastal units.

Coastal Units	Description	Pre-typhoon		Post-typhoon	
		Producer Accuracy (%)	User Accuracy (%)	Producer Accuracy (%)	User Accuracy (%)
Land	Others Land use	90.2	92.0	91.9	90.7
Wetland vegetation	Wetland vegetation	83.4	84.0	85.0	83.3
Wetland	Mudflat/tidal flat	81.4	84.7	77.1	74.0
Water	Waterbody	91.4	85.3	83.2	89.3
Overall accuracy (%)		86.5		84.3	
<i>kappa</i>		0.82		0.79	

603

604 The most remarkable gain was the wetland class after the typhoon. This is shown by an
 605 increase of wetlands from 258.14 km² to 334.97 km², i.e., an increase of 29.76% (76.83 km²)
 606 during the short periods. Furthermore, the land class has increased by only 0.20% over the
 607 typhoon period, i.e., from 45.34% (before the typhoon) to 45.44% (after the typhoon). In
 608 addition, it has been noticed the waterbody decreased by 3.09% (20.78 km²) after the typhoon.
 609 Thus, it can be inferred that most wetland vegetation and waterbody have been converted into
 610 wetlands, which caused the coastal deterioration.

611

612 Table 6. Area changes of the different coastal units during the pre-and post-typhoon periods in
613 the Mokpo coast.

Coastal Units	Area at pre-typhoon	Area at post-typhoon	Changed area
---------------	---------------------	----------------------	--------------

	km ²	%	km ²	%	km ²	%
Land	836.87	45.34	838.55	45.44	1.68	0.20
Wetland Vegetation	77.63	4.21	19.90	1.08	-57.73	-74.37
Wetland	258.14	13.99	334.97	18.15	76.83	29.76
Water	672.95	36.46	652.18	35.34	-20.78	-3.09
Total	1845.60	100.00	1845.60	100.00	---	---

614

615

616

617

618

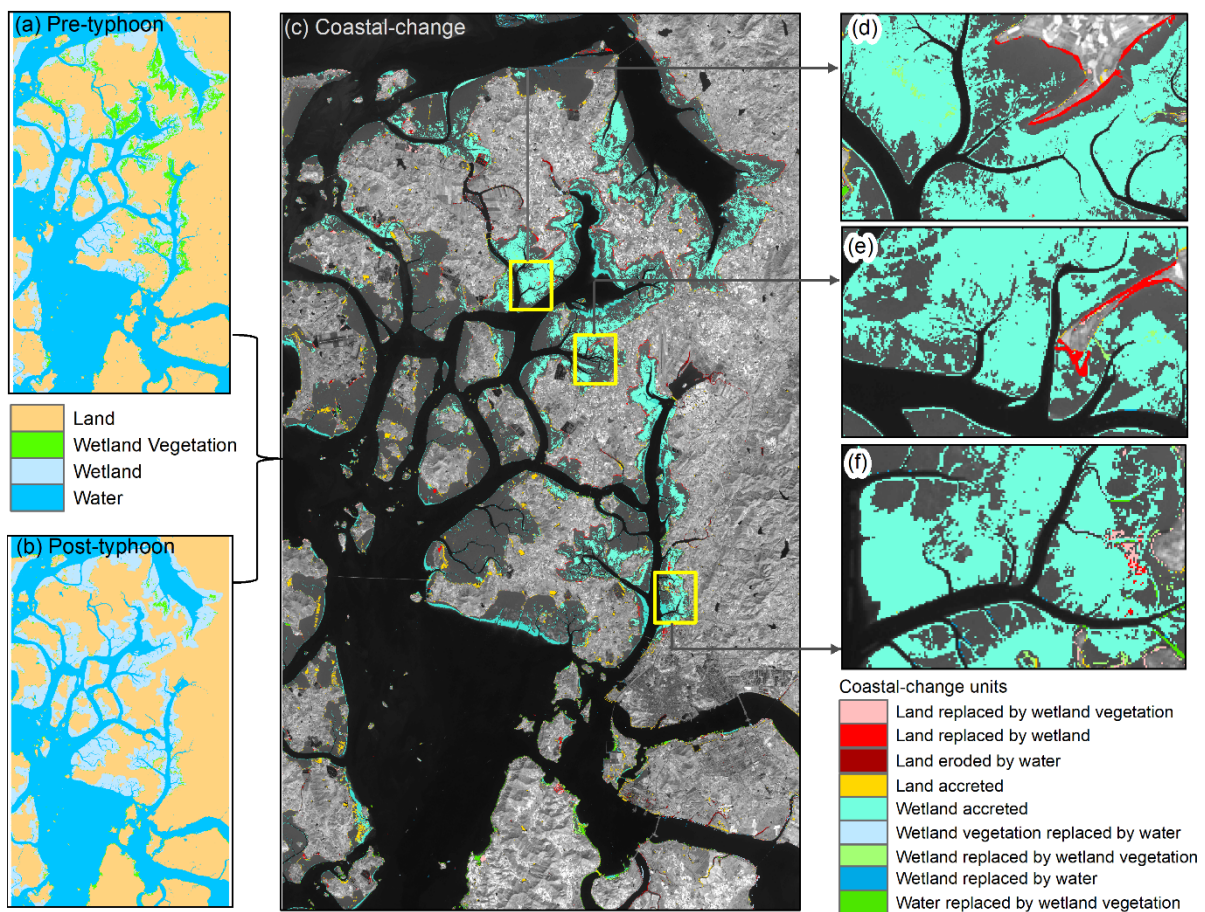
619

620

621

622

Thereafter, the coastal land transformation model was developed through mutual spatial replacements between coastal units. The land transformation model has identified the nine coastal-change units, as shown in Figure 11(c). The results show that the lowland coastal area drastically changed after the typhoon, where the majority of coastal classes have been transformed into wetlands or mudflats. Furthermore, approximately 5.61% of the land area has been replaced by wetlands and water, whereas 83.79% of the wetland area has accreted over the wetland vegetation and water due to the impact of typhoon Soulik (Table 7).



623

624

625

626

Figure 11. Spatial distribution of coastal-change units along the Mokpo coast due to typhoon Soulik: (a) pre-typhoon classified map, (b) post-typhoon classified map, and (c) coastal land transformation map. Subplots (d, e, and f) show the detailed coastal land

627 transformation.

628

629 Table 7. The details of coastal land transformation classes identify in short-period.

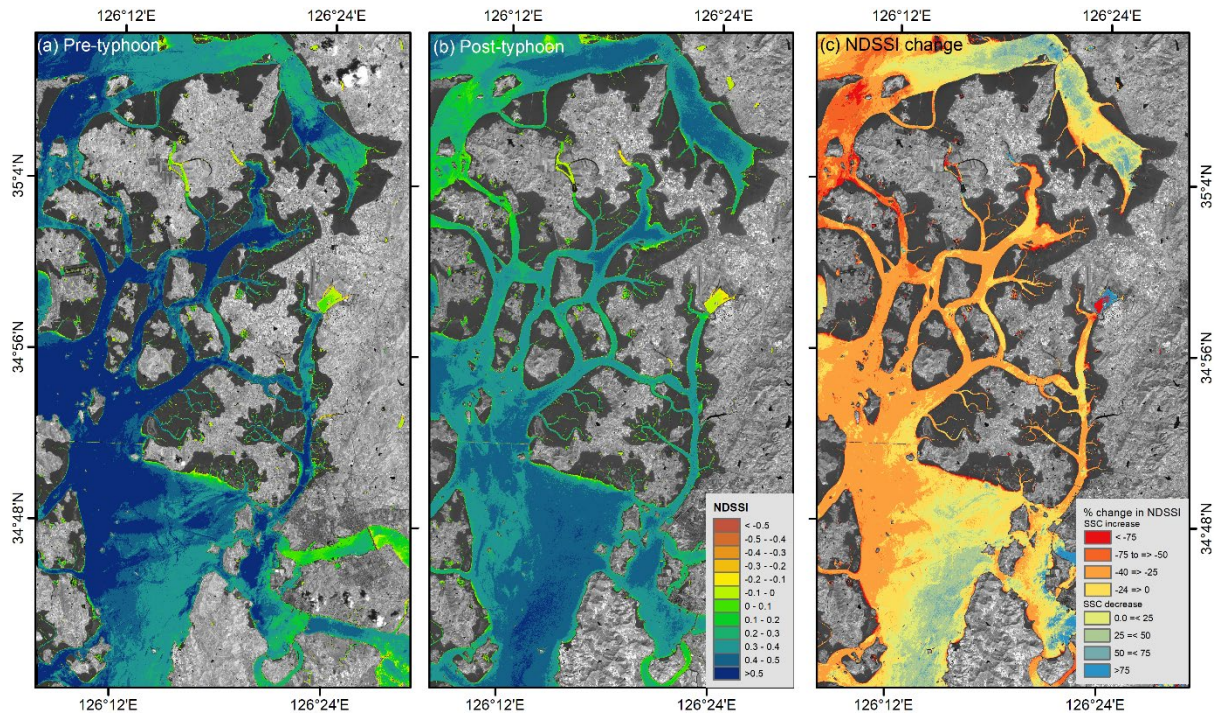
Coastal land transformation	Area (km ²)	%
Land replaced by wetland vegetation	4.59	3.94
Land replaced by wetland	4.41	3.79
Land eroded by water	2.12	1.82
Land accreted	12.88	11.06
Wetland accreted	83.79	71.97
Wetland vegetation replaced by water	2.47	2.12
Wetland replaced by wetland vegetation	1.59	1.36
Wetland replaced by water	1.76	1.52
Water replaced by wetland vegetation	2.82	2.42

630

631 4.3 Sediment resuspension during the pre-and post-typhoon period

632 The spatial distribution of relative suspended sediment concentration has been derived
633 through NDSSI for both before and after typhoon images (Fig. 12). Pre-typhoon SSC patterns
634 have been observed more SSC inside the creeks of the inner-shelf region of the Mokpo coast
635 as compared to the post-typhoon NDSSI image. However, it has been noted that the SSC has
636 significantly increased along the entire coast in the post-typhoon period (Fig. 12b). Therefore,
637 the spatial changes of relative SSC have been determined during the August (pre) and October
638 (post) periods, as depicted in Figure 12(c). In general, a flood always transports many
639 suspended materials and concentrates those materials on the upper surface of the water. After
640 the strong events, the flood-transported suspended material is deposited across the delta. A
641 similar phenomenon was observed in the post-typhoon period due to extensive rainfall, which
642 turned into a coastal flood.

643 On the other hand, it has been observed that the SSC gradually increased as the wind
644 speed increased from the pre to post-typhoon period. The increasing SSC amplitudes indicate
645 the rapid sediment erosion/resuspension over the storm passage. Furthermore, the amplitudes
646 of SSC variations were more visible in shallower water than in deeper water. The effect of
647 typhoons on the SSC variation along the Mokpo coast has been observed through Δ NDSSI
648 distribution (Fig. 12c). The negative Δ NDSSI values represent the increase of SSC due to
649 typhoon-induced strong wind and coastal flooding.

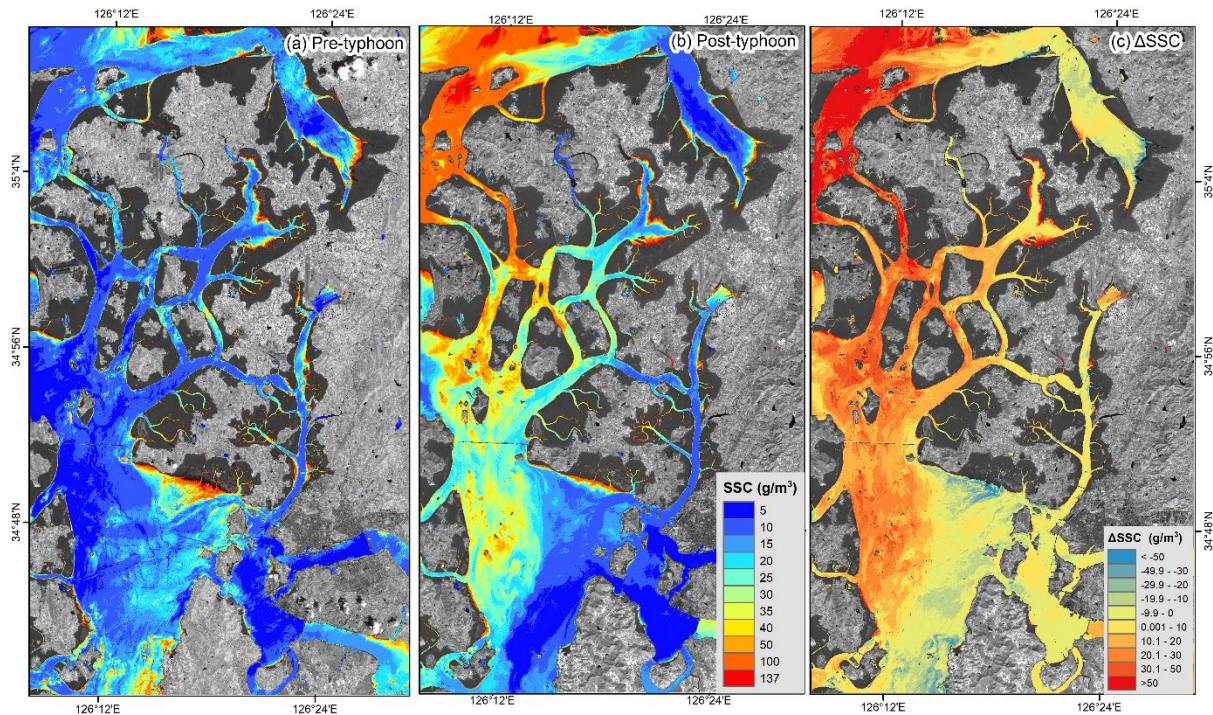


650

651 Figure 12. Relative SSC for (a) pre-typhoon and (b) post-typhoon period, while (c) represents
 652 the changes in the NDSSI.
 653

654 Furthermore, a quantitative analysis of SSC has been performed based on the algorithm
 655 developed by Choi et al. (2014). During the pre-typhoon period, the SSC in the near shore
 656 waters was significantly higher than that of the offshore region (Fig. 13a). The post-typhoon
 657 image shows a sharp increase in the SSC distribution, indicating that Typhoon Soulik
 658 significantly impacted the SSC variation, with a maximum of $>50 \text{ g/m}^3$ (Fig. 13c). In Figures
 659 13(a) and (b), the spring-neap tidal influence broadly regulated the distribution and change of
 660 SSC throughout the shallow coastal water. The resuspension of SSC has been observed in the
 661 entire study region during the passage of Soulik. The pattern of relative SSC distribution (Fig.
 662 12c) and the empirically derived SSC distribution (Fig. 13c) of pre-and post-typhoon are
 663 similar.

664 The outcomes showed that the storm surge and strong waves have considerably aided
 665 the sediment resuspension. Thus, the storm waves played an essential role in increasing bottom
 666 stress and stirring the seabed sediment (Gong and Shen, 2009). The transport of sediment
 667 during the storm adds another mechanism to the long-term morphological evolution of the
 668 Mokpo coast. This research revealed the profound significance of typhoons on inner shelf
 669 sedimentation along the coast.



670

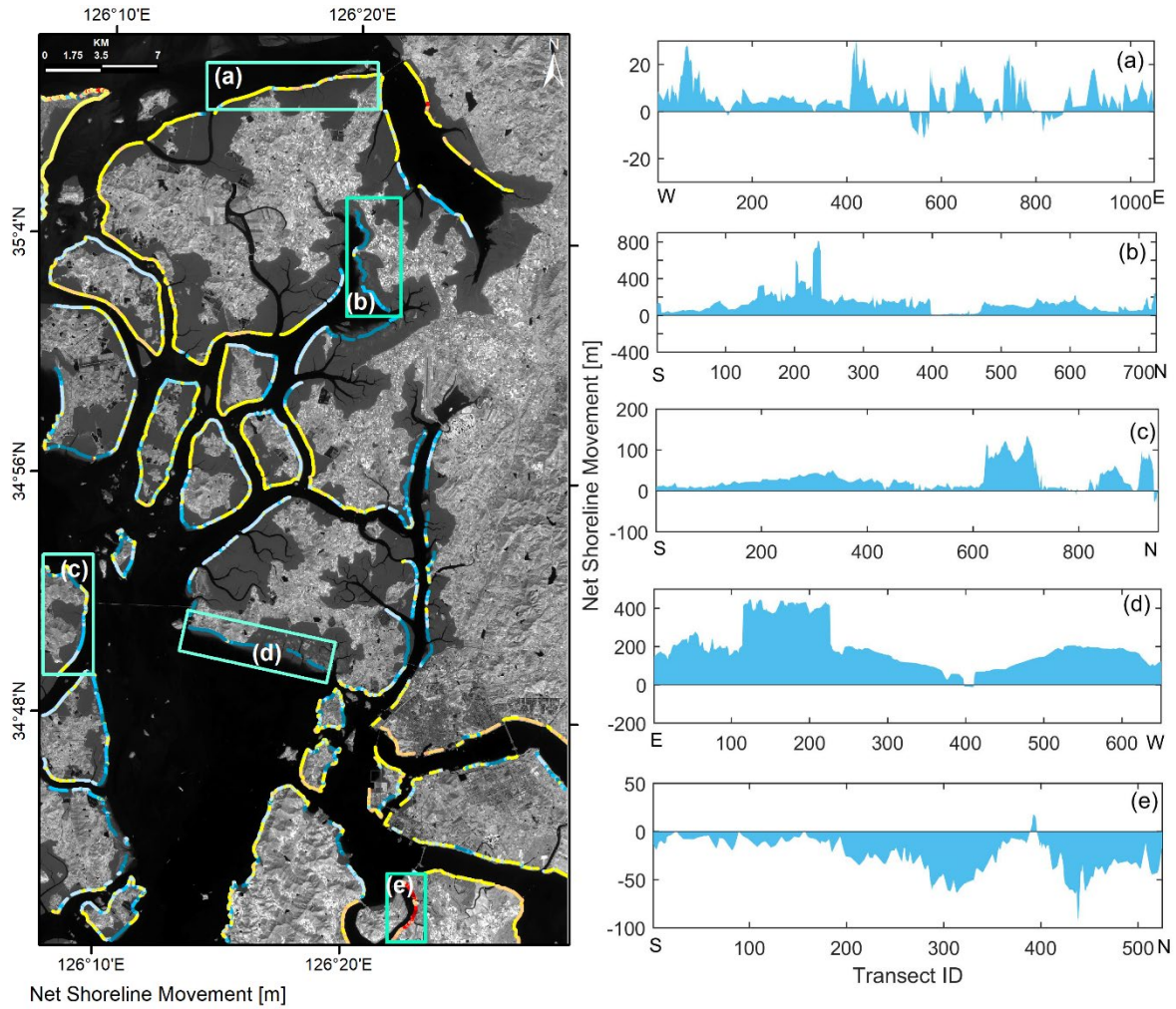
671 Figure 13. The simulated SSC distribution for the surface water of (a) pre-typhoon, (b) post-
 672 typhoon period, and (c) represents the spatial changes of SSC from pre- to post-
 673 typhoon.

674

675 4.4 Impact on coastal erosion and deposition

676

677 The impacts of the severe typhoon storm Soulik at a speed of 62 m/s on the coastline
 678 of Mokpo have been determined using the NSM method, considering 38313 transects (10m
 679 transect intervals) along the shoreline. Figure 14 shows the shoreline alteration in the entire
 680 Mokpo coastal region from the pre- to post-typhoon period (i.e., short-term), with an accretion
 681 of 87.5% transects and erosion of 12.5%. The mean deposition of 28.89m and a mean erosion
 682 of -8.29m were recorded (Table 8). The shoreline movement between 0-10m was recorded in
 683 the northern part of the coastal region. It has been observed that most transects experienced
 684 significant accretion; however, erosion has been observed in a few transects along the southern
 685 coastline (Fig. 14). The southern coast experienced sporadic landward movement of the
 686 shoreline. In contrast, the rest of the study region experienced significant seaward shoreline
 movement (Fig. 14 a-e).



687

688 Figure 14. Short-term land water boundary changes (pre- to post-typhoon period) based on the
 689 NSM method (left panel). Subplots (a-e) show the net movement of the shoreline at
 690 different sites.
 691

692 Table 8. Short-term (pre-post typhoon) shoreline change statistics based on the NSM model.

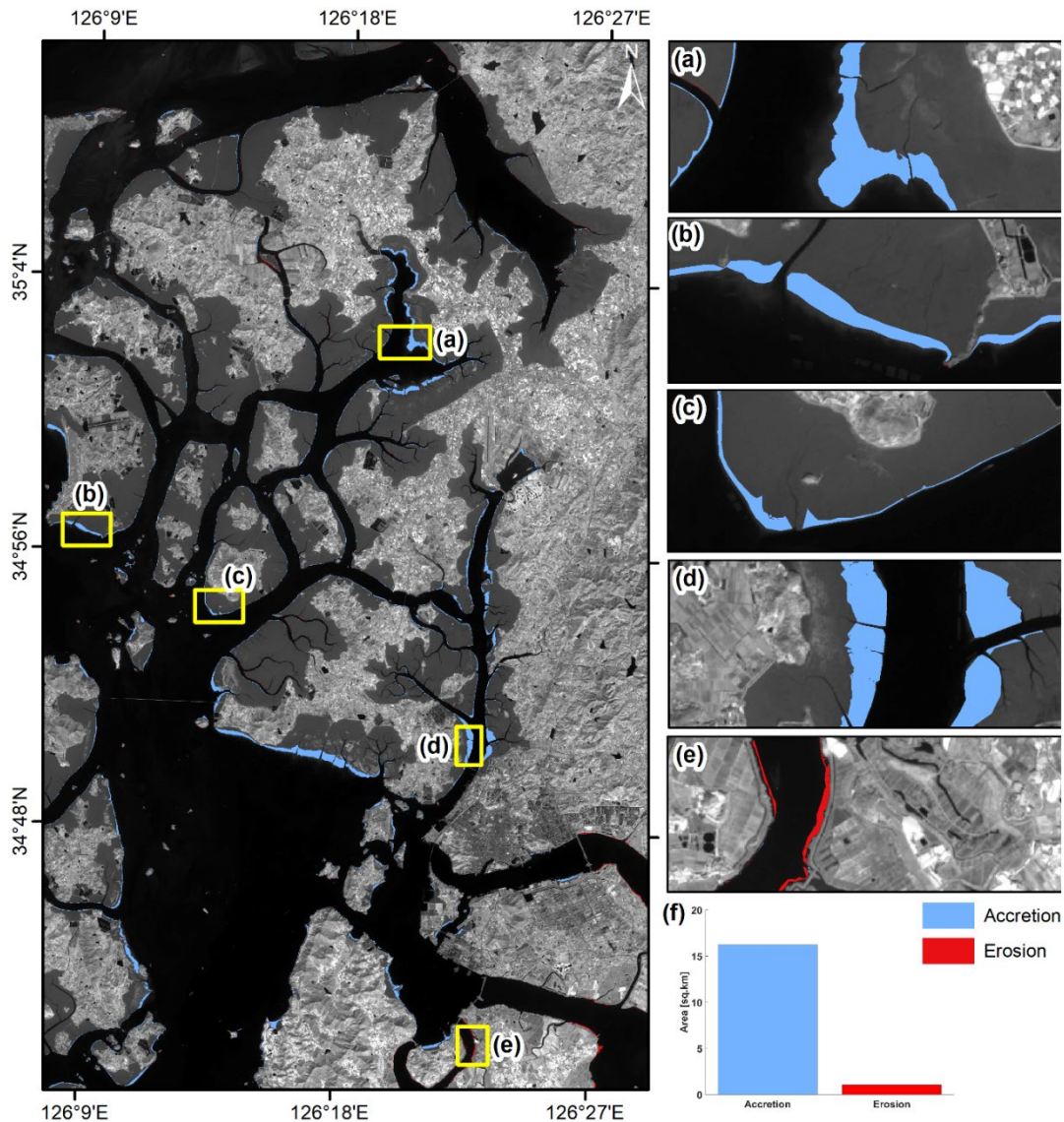
NSM statistics	Summary
Total transects	38313
NSM _{mean}	24.24m
NSM _{mean accretion}	28.89
NSM _{mean erosion}	-8.29
NSM _{maximum accretion}	812.54
NSM _{maximum erosion}	-131.72
Total transect that records accretion	34686
Total transect that records erosion	4955
% of total transect that records accretion	87.5
% of total transect that records erosion	12.5
Overall pre to post-typhoon trend	Accretion

693

694 The wind generated surface water currents that transported and dispersed erogenous
 695 material to deep seas areas from pre- to post-typhoon. On the other hand, the coastal flooding
 696 induced by the typhoon storm increased the sediment from the land to the near-shore region
 697 (Figs. 12c & 13c). This allowed sediment to deposit on the wetland or beach areas. The coastal
 698 land transformation map also revealed changes in shoreline shift-area as the wetland accreted
 699 class.

700 The net surface area changes along the coastal region have been estimated and are
 701 depicted in Figure 15. The total beach area increases and losses throughout the typhoon period
 702 were 16.23 km² and 1.1 km², respectively (Fig. 15f). It was observed that typhoon Soulik
 703 drastically increased the wetland (mudflat). These observations were also supported by other
 704 proxies, as discussed above.

705

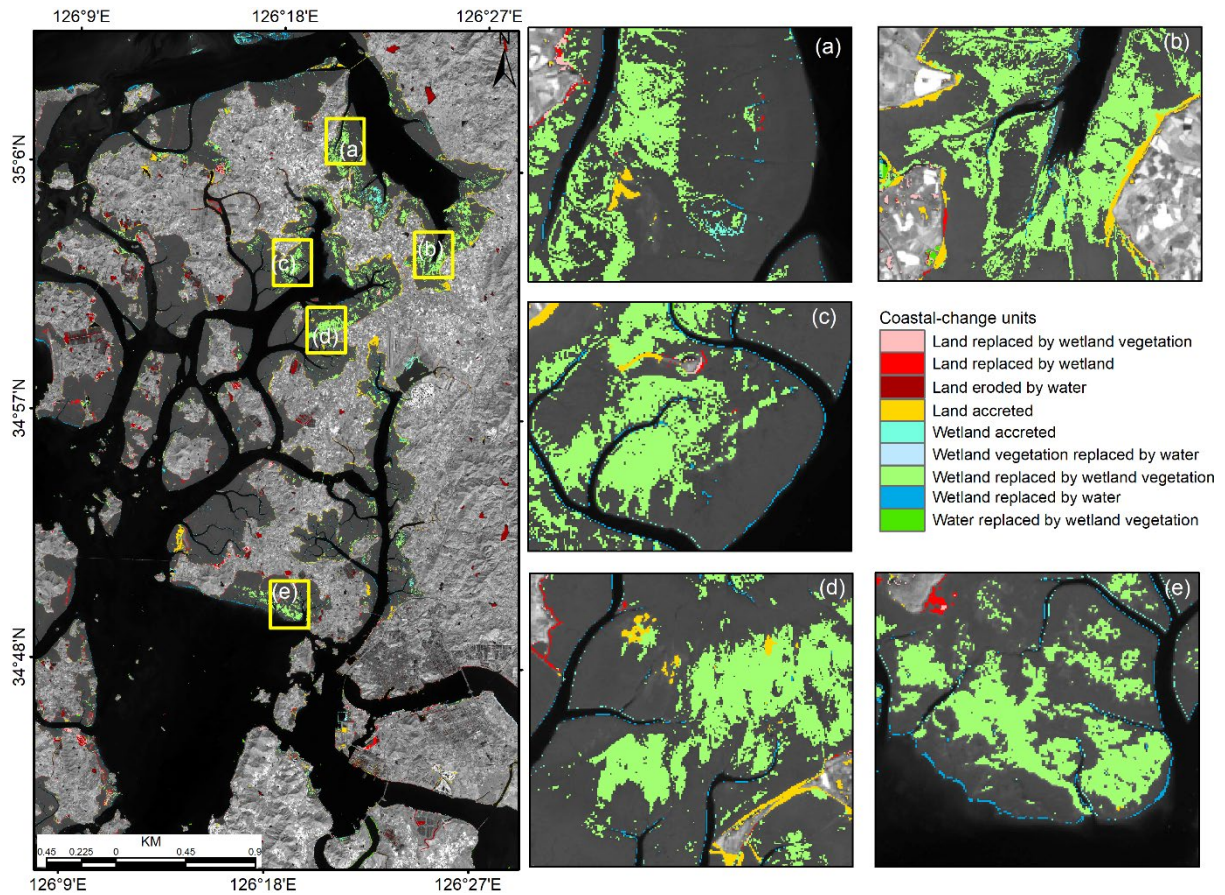


706

707 Figure 15. Short-term net surface area changes (i.e., erosion and accretion) due to typhoon
708 Soulik along the Mokpo coast. Subplots (a-d) show extensive accretion, while
709 erosion is shown in plot (e). The bar graph (f) represents the area changes from the
710 pre to post-typhoon period.
711

712 **4.5 Coastal recovery status after typhoon Soulik**

713 The recovery status, i.e., medium-term coastal changes of the Mopko coastal region
714 after typhoon Soulik has been analyzed using the NSM and coastal landform change model.
715 For this purpose, another Sentinel-2 MSI level 1C satellite image was downloaded for October
716 2019 (one year after the typhoon), as listed in Table 1. After that, the coastal landform change
717 model and NSM were performed based on the Sentinel-2 MSI images of October 2018 and
718 2019 (both images taken during the post-typhoon period) to understand the recovery status of
719 the coastal morphometry. The coastal landform change model exhibits that the wetland
720 vegetation increased drastically after one year of typhoon Soulik, as depicted in Figure 16.
721 Table 9 indicates that approximately 16.52% of the land area has accreted over the wetland and
722 water, whereas 39.71% of the wetland vegetation area has accreted over the wetland and water
723 after the typhoon. Further, the outcome of the coastal recovery status was visually compared
724 with the high-resolution aerial imagery obtained from the National Land Information Platform
725 website (<https://map.ngii.go.kr/>) and showed strong agreement. Thus, the coastal landform
726 change model successfully determined the longer-term recovery status in the topography and
727 landforms of the Mopko coastal area after the typhoon.



728
729

730 Figure 16. Recovery status of different coastal landforms after typhoon Soulik of Mokpo
731 coastal region, whereas zoom boxes (a-e) show the increase of wetland vegetation at
732 various sites.
733

734 Table 9. The details of medium-term coastal land transformation classes identify during the
735 post-typhoon period.

Coastal land transformation	Area (km ²)	%
Land replaced by wetland vegetation	4.06	6.67
Land replaced by wetland	4.59	7.54
Land eroded by water	7.23	11.88
Land accreted	10.05	16.52
Wetland accreted	2.82	4.64
Wetland vegetation replaced by water	2.12	3.48
Wetland replaced by wetland vegetation	24.17	39.71
Wetland replaced by water	4.41	7.25
Water replaced by wetland vegetation	1.41	2.32

736

737 On the other hand, the medium-term effects of a typhoon on the shoreline have also
738 been determined based on the NSM model. The results exhibit the extensive shoreline
739 alteration in the entire Mokpo coastal region after one year of typhoon Soulik, with an accretion
740 of 48.03% transects and erosion of 51.97%. The NSM statistics showed an average shoreline

741 movement of -1.08m, with a recorded mean erosion of -9.25 and deposition of 7.75m (Table
 742 10). The overall erosion was recorded in response to typhoon Soulik even after one year along
 743 the Mopko coastal region. This is due to the extensive damage to wetland vegetation during
 744 the typhoon period (Table 7). In addition, it was observed that the wetland experience accretion
 745 during the typhoon period, but it made the coastline vulnerable to erosion in the near future.
 746 The natural native vegetation and wetland vegetation play a critical role in the shoreline
 747 stability of the coastal region due to its anti-erosive nature. This phenomenon was evident in
 748 the NSM statistics obtained during the post-typhoon period. Therefore, the use of these models
 749 can help predict how the shoreline and adjacent coastal landforms will respond to typhoons,
 750 identify vulnerable areas, and inform recovery efforts. This can enhance the area's resilience to
 751 natural disasters and reduce the risk of future erosion and other environmental problems.

752
 753

Table 10. Medium-term shoreline change statistics based on the NSM model.

NSM statistics	Summary
Total transects	38313
NSM _{mean}	-1.08m
NSM _{mean accretion}	7.75
NSM _{mean erosion}	-9.25
NSM _{maximum accretion}	44.76
NSM _{maximum erosion}	-121.14
Total transect that records accretion	18400
Total transect that records erosion	19913
% of total transect that records accretion	51.97
% of total transect that records erosion	48.03
Overall pre to post-typhoon trend	Erosion

754
 755
 756

5. Conclusion

757 The objectives of this study were to assess the impact of typhoon Soulik on the coastal ecology,
 758 landform, erosion/accretion, suspended sediment movement and associated coastal changes
 759 along the Mokpo coast. This research developed an integrated approach for identifying coastal
 760 dynamics impacted by typhoons and determining damage severity. The coastline movement,
 761 coastal morphodynamics and quantified severity of vegetation damage from the pre- to post-
 762 typhoon period have been determined based on the Sentinel-2 MSI images. NDVI and FVC
 763 have been used to assess the severity of damage caused by typhoon Soulik on the vegetation.
 764 The results showed that about 493.9 km² (26.7%) of vegetation had been affected in the Mokpo
 765 coastal region. Further, it was observed that 6.1% (112.4 km²) of vegetated areas in low coastal
 766 land were severely damaged. The land transformation model exhibited that the ‘wetland’

767 replaced most of the ‘wetland-vegetated land’ in the post-typhoon period. Also, it has been
768 found that more aggregated vegetation regions were less susceptible to damage.

769 The SSC of the Mokpo coastal region is higher in the post-typhoon period compared to
770 pre-typhoon time. The SSC variation influenced the coastal accretion and changed the deltaic
771 islands. The NDSSI and empirical-based SSC distribution of pre- and post-typhoon images
772 exhibit sedimentation drastically increased after the typhoon. The land accretion process also
773 dominated during the pre- to post-typhoon period. The wetlands and water have replaced
774 approximately 9.77% of the land area. On the other hand, 65.52% of the wetland area has
775 accreted over the wetland vegetation and water. Shoreline change analysis is also performed to
776 understand erosion and accretion in coastal regions. Typhoon Soulik accelerated shoreline
777 movement, affecting the local environmental condition, biodiversity imbalance, and aerial
778 change. In addition, 87.35% of shoreline transects experienced seaward migration over the
779 typhoon period. The wetland experience accretion in a shorter period, but it makes the coastline
780 vulnerable to erosion in the near future because the natural native vegetation and wetland
781 vegetation are crucial factors in shoreline stability of the coastal region due to its anti-erosive
782 nature. This phenomenon was evident in the NSM and coastal landforms change model
783 obtained in the medium-term analysis. However, more high-resolution, cloud-free multi-
784 temporal images and in-situ observations are required to better understand the medium to long-
785 term typhoon-induced morphodynamics of the coastal region. It can be concluded that the
786 Mokpo coastal ecosystem has been devastated by this extreme event. Although the observed
787 changes are not alarming, shoreline protection measures still need to be addressed, especially
788 the reforestation in wetland or mudflat regions. The outputs of the present study are needed to
789 better understand the sediment transport process and estuary changes during the pre-and post-
790 typhoon period. It can also be used to develop appropriate strategies to protect natural
791 ecosystems and post-disaster rehabilitation.

792

793 **Acknowledgments**

794 This paper was supported by research funds for newly appointed professors of Gangneung-
795 Wonju National University in 2021. The authors are thankful to the European Space Agency
796 (ESA) for providing free satellite images. The authors would like to thank the esteemed
797 reviewers for their valuable comments and suggestions that helped improve the manuscript.

798

799 **Funding**

800 This work was supported by the National Research Foundation of Korea (NRF) grant funded
801 by the Korea government (NRF-2021R1C1C2003316) and Basic Science Research Program
802 through the National Research Foundation of Korea (NRF) funded by the Ministry of
803 Education (2021R1A6A1A03044326).

804

805 **References**

806 Abbas, S., Nichol, J. E., Fischer, G. A., Wong, M. S., and Irteza, S. M.: Impact assessment of
807 a super-typhoon on Hong Kong's secondary vegetation and recommendations for
808 restoration of resilience in the forest succession, *Agricultural and Forest Meteorology*,
809 280, 107784, <https://doi.org/10.1016/j.agrformet.2019.107784>, 2020.

810 Adhikari, M. D., Maiti, S., Bera, A., and Chaudhury, N. R.: Post-tsunami adjustment of coral
811 reef platform and other morphometric changes in Landfall Island, North Andaman—
812 An integrated field and remote sensing-based approach, *Regional Studies in Marine
813 Science*, 48, 101975, <https://doi.org/10.1016/j.rsma.2021.101975>, 2021.

814 Altman, J., Doležal, J., Černý, T., and Song, J. S.: Forest response to increasing typhoon
815 activity on the Korean peninsula: evidence from oak tree-rings, *Global Change Biology*,
816 19(2), 498-504, <https://doi.org/10.1111/gcb.12067>, 2013.

817 Amiri, R., Weng, Q., Alimohammadi, A., and Alavipanah, S. K.: Spatial-temporal dynamics
818 of land surface temperature in relation to fractional vegetation cover and land use/cover
819 in the Tabriz urban area, Iran, *Remote sensing of environment*, 113(12), 2606-2617,
820 <https://doi.org/10.1016/j.rse.2009.07.021>, 2009.

821 Arisanty, D., and Saputra, A. N.: Remote sensing studies of suspended sediment concentration
822 variation in Barito Delta, In *IOP Conference Series: Earth and Environmental Science*,
823 98(1), 012058, 2017.

824 Aswatha, S. M., Mukherjee, J., Biswas, P. K., and Aikat, S.: Unsupervised classification of
825 land cover using multi-modal data from multispectral and hybrid-polarimetric SAR
826 imageries, *International Journal of Remote Sensing*, 41(14), 5277-5304,
827 <https://doi.org/10.1080/01431161.2020.1731771>, 2020.

828 Awad, M., and El-Sayed, H. M.: The analysis of shoreline change dynamics and future
829 predictions using automated spatial techniques: Case of El-Omayed on the
830 Mediterranean coast of Egypt, *Ocean & Coastal Management*, 205, 105568,
831 <https://doi.org/10.1016/j.ocecoaman.2021.105568>, 2021.

832 Bao, A., Huang, Y., Ma, Y., Guo, H., and Wang, Y.: Assessing the effect of EWDP on

833 vegetation restoration by remote sensing in the lower reaches of Tarim River,
834 Ecological Indicators, 74, 261-275, <https://doi.org/10.1016/j.ecolind.2016.11.007>,
835 2017.

836 Bhowmik, A. K., and Cabral, P.: Cyclone Sidr impacts on the Sundarbans floristic diversity,
837 Earth Science Research, 2(2), 62, <http://dx.doi.org/10.5539/esr.v2n2p62>, 2013.

838 Bhuiyan, Md. J. A. N. and Dutta, D.: Analysis of flood vulnerability and assessment of the
839 impacts in coastal zones of Bangladesh due to potential sea-level rise, Natural Hazards,
840 61(2), 729-743, <https://doi.org/10.1007/s11069-011-0059-3>, 2012.

841 Bian, S., Hu, Z., Liu, J., and Zhu, Z.: Sediment suspension and the dynamic mechanism during
842 storms in the Yellow River Delta, Environmental Monitoring and Assessment, 189(1),
843 1-13, <https://doi.org/10.1007/s10661-016-5688-2>, 2017.

844 Bishop-Taylor, R., Nanson, R., Sagar, S., and Lymburner, L.: Mapping Australia's dynamic
845 coastline at mean sea level using three decades of Landsat imagery, Remote Sensing of
846 Environment, 267, 112734, <https://doi.org/10.1016/j.rse.2021.112734>, 2021.

847 Byun, D. S., Wang, X. H., and Holloway, P. E.: Tidal characteristic adjustment due to dyke
848 and seawall construction in the Mokpo Coastal Zone, Korea, Estuarine, Coastal and
849 Shelf Science, 59(2), 185-196, <https://doi.org/10.1016/j.ecss.2003.08.007>, 2004.

850 Cakir, H. I., Khorram, S., and Nelson, S. A.: Correspondence analysis for detecting land cover
851 change, Remote Sensing of Environment, 102 (3-4), 306-317, <https://doi.org/10.1016/j.rse.2006.02.023>, 2006.

852

853 Carlson, T. N., and Ripley, D. A.: On the relation between NDVI, fractional vegetation cover,
854 and leaf area index, Remote sensing of Environment, 62(3), 241-252,
855 [https://doi.org/10.1016/S0034-4257\(97\)00104-1](https://doi.org/10.1016/S0034-4257(97)00104-1), 1997.

856 Cha, E. J., Yun, S. G., Moon, I. J., and Kim, D. H.: Binary interaction of typhoons Soulik and
857 Cimaron in 2018–Part I: Observational characteristics and forecast error, Tropical
858 Cyclone Research and Review, 10(1), 32-42, <https://doi.org/10.1016/j.tcr.2021.03.001>, 2021.

859

860 Charrua, A. B., Padmanaban, R., Cabral, P., Bandeira, S., and Romeiras, M. M.: Impacts of the
861 tropical cyclone idai in mozambique: A multi-temporal Landsat satellite imagery
862 analysis, Remote Sensing, 13(2), 201, <https://doi.org/10.3390/rs13020201>, 2021.

863 Chau, P. M., Wang, C. K., and Huang, A. T.: The spatial-temporal distribution of GOCI-
864 derived suspended sediment in Taiwan coastal water induced by typhoon Soudelor,
865 Remote Sensing, 13(2), 194, <https://doi.org/10.3390/rs13020194>, 2021.

- 866 Choi, M. K., Choi, H. G., Moon, H. B., Yu, J., Kang, S. K., and Choi, S. K.: Sources and
867 distributions of organic wastewater compounds on the Mokpo Coast of Korea, Fisheries
868 and Aquatic Sciences, 10(4), 205-214, <https://doi.org/10.5657/fas.2007.10.4.205>, 2007.
- 869 Choi, J. K., Park, Y. J., Ahn, J. H., Lim, H. S., Eom, J., and Ryu, J. H.: GOCI, the world's first
870 geostationary ocean color observation satellite, for the monitoring of temporal
871 variability in coastal water turbidity, Journal of Geophysical Research: Oceans,
872 117(C9), <https://doi.org/10.1029/2012JC008046>, 2012.
- 873 Choi, J. K., Park, Y. J., Lee, B. R., Eom, J., Moon, J. E., and Ryu, J. H.: Application of the
874 Geostationary Ocean Color Imager (GOCI) to mapping the temporal dynamics of
875 coastal water turbidity, Remote Sensing of Environment, 146, 24-35, <https://doi.org/10.1016/j.rse.2013.05.032>, 2014.
- 876
- 877 Choi, K.: Morphology, sedimentology and stratigraphy of Korean tidal flats—Implications for
878 future coastal managements, Ocean & Coastal Management, 102, 437-448,
879 <https://doi.org/10.1016/j.ocecoaman.2014.07.009>, 2014.
- 880 Chu, T., Guo, X., and Takeda, K.: Remote sensing approach to detect post-fire vegetation
881 regrowth in Siberian boreal larch forest, Ecological Indicators, 62, 32-46,
882 <https://doi.org/10.1016/j.ecolind.2015.11.026>, 2016.
- 883 Congalton, R. G.: A review of assessing the accuracy of classifications of remotely sensed data,
884 Remote Sensing of Environment, 37(1), 35-46, [https://doi.org/10.1016/0034-4257\(91\)90048-B](https://doi.org/10.1016/0034-4257(91)90048-B), 1991.
- 885
- 886 Dai, C, Howat, I. M., Larour, E., and Husby, E.: Coastline extraction from repeat high
887 resolution satellite imagery, Remote Sensing of Environment, 229, 260–270,
888 <https://doi.org/10.1016/j.rse.2019.04.010>, 2019.
- 889 Dail, M. B., Corbett, D. R., and Walsh, J. P.: Assessing the importance of tropical cyclones on
890 continental margin sedimentation in the Mississippi delta region, Continental Shelf
891 Research, 27(14), 1857-1874, <https://doi.org/10.1016/j.csr.2007.03.004>, 2007.
- 892 Datta, D. and Deb, S.: Analysis of coastal land use/land cover changes in the Indian Sunderbans
893 using remotely sensed data, Geospatial Information Science, 15(4), 241-250,
894 <https://doi.org/10.1080/10095020.2012.714104>, 2012.
- 895 Deabes, E. A.: Applying ArcGIS to Estimate the Rates of Shoreline and Back-Shore Area
896 Changes along the Nile Delta Coast, Egypt, International Journal of Geosciences, 8(03),
897 332, [DOI: 10.4236/ijg.2017.83017](https://doi.org/10.4236/ijg.2017.83017), 2017.
- 898 Eastman, J. R., Sangermano, F., Machado, E. A., Rogan, J., and Anyamba, A.: Global trends

899 in seasonality of normalized difference vegetation index (NDVI), 1982–2011, Remote
900 Sensing, 5(10), 4799-4818, <https://doi.org/10.3390/rs5104799>, 2013.

901 Eom, J., Lee, C., Jang, J., Choi, J. K., and Park, S.: Study on environmental change monitoring
902 between shoreline change and suspended sediment concentration using Landsat images
903 in Nakdong river, Korea, In IEEE International Geoscience and Remote Sensing
904 Symposium (IGARSS), 3607-3609, 2017.

905 ERDAS.: ERDAS Imagine Tour Guides (Atlanta, GA: ERDAS Inc.), 1997.

906 ESA.: Multispectral instrument (MSI) overview, Retrieved 07th September, 2022, from
907 <https://sentinels.copernicus.eu/web/sentinel/technical-guides/sentinel-2-msi>, 2020.

908 Filgueiras, R., Mantovani, E. C., Althoff, D., Fernandes Filho, E. I., and Cunha, F. F. D.: Crop
909 NDVI monitoring based on sentinel 1, Remote Sensing, 11(12), 1441, [https://doi.org](https://doi.org/10.3390/rs11121441)
910 [/10.3390/rs11121441](https://doi.org/10.3390/rs11121441), 2019.

911 Ge, J., Meng, B., Liang, T., Feng, Q., Gao, J., Yang, S., ... and Xie, H.: Modeling alpine
912 grassland cover based on MODIS data and support vector machine regression in the
913 headwater region of the Huanghe River, China, Remote Sensing of Environment, 218,
914 162-173, <https://doi.org/10.1016/j.rse.2018.09.019>, 2018.

915 Goff, J. A., Allison, M. A., and Gulick, S. P.: Offshore transport of sediment during cyclonic
916 storms: Hurricane Ike (2008), Texas Gulf Coast, USA, Geology, 38(4), 351-354,
917 <https://doi.org/10.1130/G30632.1>, 2010.

918 Gong, W. and Shen, J.: Response of sediment dynamics in the York River Estuary, USA to
919 tropical cyclone Isabel of 2003, Estuarine, Coastal and Shelf Science, 84(1), 61-74,
920 <https://doi.org/10.1016/j.ecss.2009.06.004>, 2009.

921 Halder, B. and Bandyopadhyay, J.: Monitoring the tropical cyclone ‘Yass’ and
922 ‘Amphan’ affected flood inundation using Sentinel-1/2 data and Google Earth Engine,
923 Modeling Earth Systems and Environment, 1-16, [https://doi.org/10.1007/s40808-022-](https://doi.org/10.1007/s40808-022-01359-w)
924 [01359-w](https://doi.org/10.1007/s40808-022-01359-w), 2022.

925 Hopper, M.: WXTide32 Version 4.0. Free Software Foundation Inc., Cambridge, 2004.

926 Hoque, M. A. A., Phinn, S., Roelfsema, C., and Childs, I.: Assessing tropical cyclone impacts
927 using object-based moderate spatial resolution image analysis: a case study in
928 Bangladesh, International Journal of Remote Sensing, 37(22), 5320-5343,
929 <https://doi.org/10.1080/01431161.2016.1239286>, 2016.

930 Hossain, A. K. M. A., Jia, Y., and Chao, X.: Development of remote sensing based index for
931 estimating/mapping suspended sediment concentration in river and lake environments,

932 In Proceedings of 8th international symposium on ECOHYDRAULICS, 435, 578-585,
933 2010.

934 Hossain, A. A., Mathias, C., and Blanton, R.: Remote sensing of turbidity in the Tennessee
935 River using Landsat 8 satellite, *Remote Sensing*, 13(18), 3785, [https://doi.org/
936 10.3390/rs13183785](https://doi.org/10.3390/rs13183785), 2021.

937 Hu, T. and Smith, R. B.: The impact of Hurricane Maria on the vegetation of Dominica and
938 Puerto Rico using multispectral remote sensing, *Remote Sensing*, 10(6), 827,
939 <https://doi.org/10.3390/rs10060827>, 2018.

940 Hwang, D. J., Choi, J. K., Eom, J., Ryu, J. H., and Woo, H. J.: Long-term monitoring of
941 suspended sediments concentration using GOCI and field data in Han-river estuary,
942 Korea, In 2016 IEEE International Geoscience and Remote Sensing Symposium, 2465-
943 2467, 2016.

944 Hwang, S., Son, S., Lee, C., and Yoon, H. D.: Quantitative assessment of inundation risks from
945 physical contributors associated with future storm surges: a case study of Typhoon
946 Maemi (2003), *Natural Hazards*, 104(2), 1389-1411, [https://doi.org/10.1007/s11069-
947 020-04225-z](https://doi.org/10.1007/s11069-020-04225-z), 2020.

948 Jing, X., Yao, W. Q., Wang, J. H., and Song, X. Y.: A study on the relationship between
949 dynamic change of vegetation coverage and precipitation in Beijing's mountainous
950 areas during the last 20 years, *Mathematical and Computer Modelling*, 54(3-4), 1079-
951 1085, <https://doi.org/10.1016/j.mcm.2010.11.038>, 2011.

952 Kang, J. W.: Changes in tidal characteristics as a result of the construction of sea-dike/sea-
953 walls in the Mokpo coastal zone in Korea, *Estuarine, Coastal and Shelf Science*, 48 (4),
954 429-438, <https://doi.org/10.1006/ecss.1998.0464>, 1999.

955 Kang, J. W. and Jun, K. S.: Flood and ebb dominance in estuaries in Korea, *Estuarine, Coastal
956 and Shelf Science*, 56 (1), 187-196, [https://doi.org/10.1016/S0272-7714\(02\)00156-7](https://doi.org/10.1016/S0272-7714(02)00156-7),
957 2003.

958 Kang, J. W., Moon, S. R., Lee, D. S., and Lee, J. L.: Surge-Wave Combined Inundation at
959 Mokpo North Harbour, Korea, *Journal of Coastal Research*, 1081-1085, 2007.

960 Kang, K., Jo, H. J., and Kim, Y.: Ocean responses to Typhoon Soulik (1819) around Korea,
961 *Ocean Science Journal*, 55(3), 445-457, <https://doi.org/10.1007/s12601-020-0030-x>,
962 2020.

963 Kang, K. and Moon, I. J.: Sea Surface Height Changes due to the Tropical Cyclone-Induced
964 Water Mixing in the Yellow Sea, Korea, *Frontiers of Earth Science*, 10, 826582, [doi:
https://doi.org/10.1007/s11464-019-0758-8](https://doi.org/10.1007/s11464-019-0758-8)

965 [10.3389/feart.2022.826582](https://doi.org/10.3389/feart.2022.826582), 2022.

966 Kavan, J., Wieczorek, I., Tallentire, G. D., Demidionov, M., Uher, J., and Strzelecki, M. C.:
967 Estimating Suspended Sediment Fluxes from the Largest Glacial Lake in Svalbard to
968 Fjord System Using Sentinel-2 Data: Trebrevatnet Case Study, *Water*, 14(12), 1840,
969 <https://doi.org/10.3390/w14121840>, 2022.

970 Kermani, S., Boutiba, M., Guendouz, M., Guettouche, M. S., and Khelfani, D.: Detection and
971 analysis of shoreline changes using geospatial tools and automatic computation: Case
972 of jijelian sandy coast (East Algeria), *Ocean & Coastal Management*, 132, 46-58,
973 <https://doi.org/10.1016/j.ocecoaman.2016.08.010>, 2016.

974 Keukelaere, L. De, Sterckx, S., Adriaensen, S., Knaeps, E., Reusen, I., Giardino, C., ... and
975 Vaiciute, D.: Atmospheric correction of Landsat-8/OLI and Sentinel-2/MSI data using
976 iCOR algorithm: validation for coastal and inland waters, *European Journal of Remote*
977 *Sensing*, 51(1), 525-542, <https://doi.org/10.1080/22797254.2018.1457937>, 2018.

978 Kim, Y. C.: *Handbook of coastal and ocean engineering*, World Scientific, 2010.

979 Kim, J. M., Bae, J., Son, S., Son, K., and Yum, S. G.: Development of model to predict natural
980 disaster-induced financial losses for construction projects using deep learning
981 techniques. *Sustainability*, 13(9), 5304, <https://doi.org/10.3390/su13095304>, 2021.

982 KMA.: Typhoon White Book, Available at https://www.kma.go.kr/download_01
983 [/typhoon/typwhitebook_2011.pdf](https://www.kma.go.kr/download_01/typhoon/typwhitebook_2011.pdf), 2011.

984 KMA.: 2018 annual report, available at https://www.kma.go.kr/download_01/Annual
985 [_Report_2018.pdf](https://www.kma.go.kr/download_01/Annual_Report_2018.pdf), 2018.

986 Konda, V. G. R. K., Chejarla, V. R., Mandla, V. R., Voleti, V., and Chokkavarapu, N.:
987 Vegetation damage assessment due to Hudhud cyclone based on NDVI using Landsat-
988 8 satellite imagery, *Arabian Journal of Geosciences*, 11(2), 1-11,
989 <https://doi.org/10.1007/s12517-017-3371-8>, 2018.

990 Kumar, R., Rani, S., and Maharana, P.: Assessing the impacts of Amphan cyclone over West
991 Bengal, India: a multi-sensor approach, *Environmental Monitoring and Assessment*,
992 193(5), 1-21, <https://doi.org/10.1007/s10661-021-09071-5>, 2021.

993 Kwon, J. I., Choi, J. W., Lee, J. C., Min, I. K., and Park, K. S.: Spatio-temporal Characteristics
994 of Storm Surge Events in the Korean Peninsula, *Journal of Coastal Research*, 85
995 (10085), 891-895, 2018.

996 Landis, J. R. and Koch, G. G.: An application of hierarchical kappa-type statistics in the
997 assessment of majority agreement among multiple observers, *Biometrics*, 363-374,

998 1977.

999 Lee, J. K., Kim, J. O., and Oh, Y. S.: Development of Coastal Safety Mapping System by
1000 Vulnerability Assessment of Tidal Creeks, *Journal of Coastal Research*, 114, 459-463,
1001 2021.

1002 Lee, M. S., Park, K., Chung, J. Y., Ahn, Y. H., and Moon, J. E.: Estimation of coastal suspended
1003 sediment concentration using satellite data and oceanic in-situ measurements, *Korean
1004 Journal of Remote Sensing*, 27(6), 677-692, 2011.

1005 Lee, S. W., Nam, S. H., and Kim, D. J.: Estimation of marine winds in and around typhoons
1006 using multi-platform satellite observations: Application to Typhoon Soulik (2018),
1007 *Frontiers of Earth Science*, 16(1), 175-189, [https://doi.org/10.1007/s11707-020-0849-](https://doi.org/10.1007/s11707-020-0849-6)
1008 [6](https://doi.org/10.1007/s11707-020-0849-6), 2022.

1009 Lee, Y.: 2014. Coastal planning strategies for adaptation to sea level rise: A case study of
1010 Mokpo, Korea, *Journal of Building Construction and Planning Research*, 2(1),
1011 [DOI:10.4236/jbcpr.2014.21007](https://doi.org/10.4236/jbcpr.2014.21007), 2014.

1012 Lee, Y. K., Choi, J. K., and Lee, H. J.: A study on seasonal dynamics of suspended particulate
1013 matter in Korean coastal waters using GOCI, *Journal of Coastal Research*, 102 (SI),
1014 232-245, <https://doi.org/10.2112/SI102-029.1>, 2020.

1015 Li, K. and Li, G. S.: Risk assessment on storm surges in the coastal area of Guangdong
1016 Province, *Natural Hazards*, 68(2), 1129-1139, [https://doi.org/10.1007/s11069-013-](https://doi.org/10.1007/s11069-013-0682-2)
1017 [0682-2](https://doi.org/10.1007/s11069-013-0682-2), 2013.

1018 Li, Y., Li, H., Qiao, L., Xu, Y., Yin, X., and He, J.: Storm deposition layer on the Fujian coast
1019 generated by Typhoon Saola (2012), *Scientific reports*, 5(1), 1-7,
1020 <https://doi.org/10.1038/srep14904>, 2015.

1021 Li, Y. and Li, X.: Remote sensing observations and numerical studies of a super typhoon-
1022 induced suspended sediment concentration variation in the East China Sea, *Ocean
1023 Modelling*, 104, 187-202, <https://doi.org/10.1016/j.ocemod.2016.06.010>, 2016.

1024 Liu, Y., Wu, L., and Yue, H.: Biparabolic NDVI-Ts space and soil moisture remote sensing in
1025 an arid and semi-arid area, *Canadian Journal of Remote Sensing*, 41(3), 159-169,
1026 <https://doi.org/10.1080/07038992.2015.1065705>, 2015.

1027 Lu, J., Jiang, J., Li, A., and Ma, X.: Impact of Typhoon Chan-hom on the marine environment
1028 and sediment dynamics on the inner shelf of the East China Sea: In-situ seafloor
1029 observations, *Marine Geology*, 406, 72-83, [https://doi.org/10.1016/j.margeo.](https://doi.org/10.1016/j.margeo.2018.09.009)
1030 [2018.09.009](https://doi.org/10.1016/j.margeo.2018.09.009), 2018.

- 1031 Lu, L., Wu, C., and Di, L.: Exploring the spatial characteristics of typhoon-induced vegetation
1032 damages in the southeast coastal area of China from 2000 to 2018, *Remote Sensing*,
1033 12(10), 1692, <https://doi.org/10.3390/rs12101692>, 2020.
- 1034 Lugo, A. E., Applefield, M., Pool, D. J., and McDonald, R. B.: The impact of Hurricane David
1035 on the forests of Dominica, *Canadian Journal of Forest Research*, 13(2), 201-211,
1036 <https://doi.org/10.1139/x83-029>, 1983.
- 1037 Maiti, S., and Bhattacharya, A. K.: Shoreline change analysis and its application to prediction:
1038 A remote sensing and statistics based approach, *Marine Geology* 257(1-4), 11-23,
1039 <https://doi.org/10.1016/j.margeo.2008.10.006>, 2009.
- 1040 Maiti, S. and Bhattacharya, A. K.: A three-unit-based approach in coastal-change studies using
1041 Landsat images, *International Journal of Remote Sensing*, 32(1), 209-229,
1042 <https://doi.org/10.1080/01431160903439965>, 2011.
- 1043 Mallick, B., Ahmed, B., and Vogt, J.: Living with the risks of cyclone disasters in the
1044 southwestern coastal region of Bangladesh, *Environments*, 4(1), 13,
1045 <https://doi.org/10.3390/environments4010013>, 2017.
- 1046 McFeeters, S. K.: The use of the Normalized Difference Water Index (NDWI) in the
1047 delineation of open water features, *International Journal of Remote Sensing*, 17(7),
1048 1425–1432, <https://doi.org/10.1080/01431169608948714>, 1996.
- 1049 Member Report: Member Report, Republic of Korea. ESCAP/WMO Typhoon Committee, 13th
1050 Integrated Workshop, Chiang Mai, Thailand, 5-9 November 2018 (Avialable at
1051 <https://www.typhooncommittee.org/13IWS/Members13IWS.html>, lat access 28th
1052 April, 2023), 2018.
- 1053 Min, J. E., Ryu, J. H., Ahn, Y. H., and Lee, K. S.: Monitoring suspended sediment distribution
1054 using Landsat TM/ETM+ data in coastal waters of Seamangeum, Korea, In *Proceedings*
1055 *of the KSRS Conference*, The Korean Society of Remote Sensing, 340-343, 2004.
- 1056 Min, J. E., Ahn, Y. H., Lee, K. S., and Ryu, J. H.: Development of Suspended Sediment
1057 Algorithm for Landsat TM/ETM+ in Coastal Sea Waters-A Case Study in Saemangeum
1058 Area, *Korean Journal of Remote Sensing*, 22(2), 87-99, 2006.
- 1059 Min, J. E., Ryu, J. H., Lee, S., and Son, S.: Monitoring of suspended sediment variation using
1060 Landsat and MODIS in the Saemangeum coastal area of Korea, *Marine Pollution*
1061 *Bulletin*, 64(2), 382-390, <https://doi.org/10.1016/j.marpolbul.2011.10.025>, 2012.
- 1062 Min, J. E., Choi, J. K., Yang, H., Lee, S., and Ryu, J. H.: Monitoring changes in suspended
1063 sediment concentration on the southwestern coast of Korea, *Journal of Coastal*

1064 Research, 70, 133-138, 2014.

1065 Mishra, M., Acharyya, T., Santos, C. A. G., da Silva, R. M., Kar, D., Kamal, A. H. M., and
 1066 Raulo, S.: Geo-ecological impact assessment of severe cyclonic storm Amphan on
 1067 Sundarban mangrove forest using geospatial technology, *Estuarine, Coastal and Shelf
 1068 Science*, 260, 107486, <https://doi.org/10.1016/j.ecss.2021.107486>, 2021a.

1069 Mishra, M., Santos, C. A. G., da Silva, R. M., Rana, N. K., Kar, D., and Parida, N. R.:
 1070 Monitoring vegetation loss and shoreline change due to tropical cyclone Fani using
 1071 Landsat imageries in Balukhand-Konark Wildlife Sanctuary, India, *Journal of Coastal
 1072 Conservation*, 25(6), 1-11, <https://doi.org/10.1007/s11852-021-00840-5>, 2021b.

1073 Moon, I. J., Oh, I. S., Murty, T., and Youn, Y. H.: Causes of the unusual coastal flooding
 1074 generated by Typhoon Winnie on the west coast of Korea, *Natural Hazards*, 29(3), 485-
 1075 500, <https://doi.org/10.1023/A:1024798718572>, 2003.

1076 Na, C. K.: Heavy metals in sediments and organisms from tidal flats along the Mokpo coastal
 1077 area, *Economic and Environmental Geology*, 37(3), 335-345, 2004.

1078 Nandi, G., Neogy, S., Roy, A. K., and Datta, D.: Immediate disturbances induced by tropical
 1079 cyclone Fani on the coastal forest landscape of eastern India: A geospatial analysis,
 1080 *Remote Sensing Applications: Society and Environment*, 20, 100407,
 1081 <https://doi.org/10.1016/j.rsase.2020.100407>, 2020.

1082 Nayak, S.: Use of satellite data in coastal mapping, *Indian Cartographer*, 22(147-157), 1, 2002.

1083 NGII.: Digital elevation model, NGII (National Geographical Information Institute), the
 1084 Ministry of Land, Infrastructure and Transport, Korea, 2018.

1085 Parida, B. R., Behera, S. N., Oinam, B., Patel, N. R., and Sahoo, R. N.: Investigating the effects
 1086 of episodic Super-cyclone 1999 and Phailin 2013 on hydro-meteorological parameters
 1087 and agriculture: An application of remote sensing, *Remote Sensing Applications:
 1088 Society and Environment*, 10, 128-137, <https://doi.org/10.1016/j.rsase.2018.03.010>,
 1089 2018.

1090 Park, J. H., Yeo, D. E., Lee, K., Lee, H., Lee, S. W., Noh, S., ..., and Nam, S.: Rapid decay of
 1091 slowly moving Typhoon Soulik (2018) due to interactions with the strongly stratified
 1092 northern East China Sea, *Geophysical Research Letters*, 46(24), 14595-14603,
 1093 <https://doi.org/10.1029/2019GL086274>, 2019.

1094 Phiri, D., Simwanda, M., and Nyirenda, V.: Mapping the impacts of cyclone Idai in
 1095 Mozambique using Sentinel-2 and OBIA approach, *South African Geographical
 1096 Journal*, 103(2), 237-258, <https://doi.org/10.1080/03736245.2020.1740104>, 2021.

- 1097 Rodgers, J. C., Murrah, A. W., and Cooke, W. H.: The impact of Hurricane Katrina on the
1098 coastal vegetation of the Weeks Bay Reserve, Alabama from NDVI data, *Estuaries and*
1099 *Coasts*, 32(3), 496-507, <https://doi.org/10.1007/s12237-009-9138-z>, 2009.
- 1100 Rouse, J. W., Haas, J. R. H., Schell, J. A., and Deering, D. W.: Monitoring vegetation systems
1101 in the Great Plains with ERTS, In *Proceedings of the 3rd ERTS Symposium*,
1102 Washington, DC, USA, 1, 1974.
- 1103 Ryang, W. H., Kang, S. I., and Cho, K. S.: Characteristics of Surface Topography and
1104 Sediments before and after the Typhoon Soulik in 2018, Macrotidal Coast of Gochang,
1105 Korea, In *AGU Fall Meeting Abstracts*, OS33B-02, 2021.
- 1106 Sadik, M., Nakagawa, H., Rahman, M., Shaw, R., Kawaike, K., and Parvin, G. A.: Assessment
1107 of cyclone Aila recovery progress in Bangladesh: a comparison between rice and
1108 shrimp farming villages in Koyra, In *Water, Flood Management and Water Security*
1109 *Under a Changing Climate*, Springer, Cham, 109-124, 2020.
- 1110 Sahoo, B. and Bhaskaran, P. K.: Multi-hazard risk assessment of coastal vulnerability from
1111 tropical cyclones—A GIS based approach for the Odisha coast, *Journal of*
1112 *Environmental Management*, 206, 1166-1178, [https://doi.org/10.1016/j.jenvman.](https://doi.org/10.1016/j.jenvman.2017.10.075)
1113 [2017.10.075](https://doi.org/10.1016/j.jenvman.2017.10.075), 2018.
- 1114 Santos, C. A. G., do Nascimento, T. V. M., Mishra, M., and da Silva, R. M.: Analysis of long-
1115 and short-term shoreline change dynamics: A study case of João Pessoa city in Brazil,
1116 *Science of the Total Environment*, 769, 144889, [https://doi.org/10.1016/j.scitotenv.](https://doi.org/10.1016/j.scitotenv.2020.144889)
1117 [2020.144889](https://doi.org/10.1016/j.scitotenv.2020.144889), 2021.
- 1118 Schneider, A.: Monitoring land cover change in urban and peri-urban areas using dense time
1119 stacks of Landsat satellite data and a data mining approach, *Remote Sensing of*
1120 *Environment*, 124, 689-704, <https://doi.org/10.1016/j.rse.2012.06.006>, 2012.
- 1121 Shahzad, M. I., Meraj, M., Nazeer, M., Zia, I., Inam, A., Mehmood, K., and Zafar, H.:
1122 Empirical estimation of suspended solids concentration in the Indus Delta Region using
1123 Landsat-7 ETM+ imagery, *Journal of Environmental Management*, 209, 254-261.,
1124 <https://doi.org/10.1016/j.jenvman.2017.12.070>, 2018.
- 1125 Shamsuzzoha, M., Noguchi, R., and Ahamed, T.: Damaged area assessment of cultivated
1126 agricultural lands affected by cyclone bulbul in coastal region of Bangladesh using
1127 Landsat 8 OLI and TIRS datasets, *Remote Sensing Applications: Society and*
1128 *Environment*, 23, 100523, <https://doi.org/10.1016/j.rsase.2021.100523>, 2021.
- 1129 Sobrino, J. A., Jiménez-Muñoz, J. C., and Paolini, L.: Land surface temperature retrieval from

1130 LANDSAT TM 5, Remote Sensing of Environment, 90(4), 434-440, [https://doi.org/](https://doi.org/10.1016/j.rse.2004.02.003)
1131 [10.1016/j.rse.2004.02.003](https://doi.org/10.1016/j.rse.2004.02.003), 2004.

1132 Son, S., Kim, Y. H., Kwon, J. I., Kim, H. C., and Park, K. S.: Characterization of spatial and
1133 temporal variation of suspended sediments in the Yellow and East China Seas using
1134 satellite ocean color data, GIScience & Remote Sensing, 51(2), 212-226,
1135 <https://doi.org/10.1080/15481603.2014.895580>, 2014.

1136 Song, W., Mu, X., Ruan, G., Gao, Z., Li, L., and Yan, G.: Estimating fractional vegetation
1137 cover and the vegetation index of bare soil and highly dense vegetation with a
1138 physically based method, International journal of applied earth observation and
1139 geoinformation, 58, 168-176, <https://doi.org/10.1016/j.jag.2017.01.015>, 2017.

1140 Souza, A. J., Dickey, T. D., and Chang, G. C.: Modeling water column structure and suspended
1141 particulate matter on the Middle Atlantic continental shelf during the passages of
1142 Hurricanes Edouard and Hortense, Journal of Marine Research, 59(6), 1021-1045,
1143 <https://doi.org/10.1357/00222400160497751>, 2001.

1144 Story, M. and Congalton, R. G.: Accuracy assessment: a user's perspective, Photogrammetric
1145 Engineering and Remote Sensing, 52(3), 397-399, 1986.

1146 Tang, R., Shen, F., Ge, J., Yang, S., and Gao, W.: Investigating typhoon impact on SSC through
1147 hourly satellite and real-time field observations: A case study of the Yangtze Estuary,
1148 Continental Shelf Research, 224, 104475, <https://doi.org/10.1016/j.csr.2021.104475>,
1149 2021.

1150 Thieler, E. R., Himmelstoss, E. A., Zichichi, J. L., and Ergul, A.: The Digital Shoreline
1151 Analysis System (DSAS) version 4.0-an ArcGIS extension for calculating shoreline
1152 change (No. 2008-1278), US Geological Survey, 2009.

1153 Tian, Y., Mingming, J., Zongming, W., Dehua, M., Baojia, D., and Chao, W.: Monitoring
1154 invasion process of *Spartina alterniflora* by seasonal Sentinel-2 imagery and an object-
1155 based random forest classification, Remote Sensing, 12(9), 1383, [https://doi.org/](https://doi.org/10.3390/rs12091383)
1156 [10.3390/rs12091383](https://doi.org/10.3390/rs12091383), 2020.

1157 Tsai, C. H., Tzang, S. Y., Hsiao, S. S., Cheng, C. C., and Li, H. W.: Coastal structure failures
1158 and coastal waves on the north coast of Taiwan due to typhoon Herb, Journal of Coastal
1159 Research, 22(2), 393-405, 2006.

1160 Tsai, Y. L. S.: Monitoring 23-year of shoreline changes of the Zengwun Estuary in Southern
1161 Taiwan using time-series Landsat data and edge detection techniques, Science of The
1162 Total Environment, 156310, <https://doi.org/10.1016/j.scitotenv.2022.156310>, 2022.

- 1163 Wang, W., Qu, J. J., Hao, X., Liu, Y., and Stanturf, J. A.: Post-hurricane forest damage
1164 assessment using satellite remote sensing, *Agricultural and forest meteorology*, 150(1),
1165 122-132, <https://doi.org/10.1016/j.agrformet.2009.09.009>, 2010.
- 1166 Wang, T., Liu, G., Gao, L., Zhu, L., Fu, Q., and Li, D.: Biological and nutrient responses to a
1167 typhoon in the Yangtze Estuary and the adjacent sea, *Journal of Coastal Research*,
1168 32(2), 323-332, 2016.
- 1169 Wang, M. and Xu, H.: Remote sensing-based assessment of vegetation damage by a strong
1170 typhoon (Meranti) in Xiamen Island, China, *Natural Hazards*, 93(3), 1231-1249,
1171 <https://doi.org/10.1007/s11069-018-3351-7>, 2018.
- 1172 Wang, S., Mu, L., Qi, M., Yu, Z., Yao, Z., and Zhao, E.: Quantitative risk assessment of storm
1173 surge using GIS techniques and open data: A case study of Daya Bay Zone, China,
1174 *Journal of Environmental Management*, 289, 112514, <https://doi.org/10.1016/j.jenvman.2021.112514>, 2021.
- 1175
- 1176 WMO (World Meteorological Organization): Tropical cyclones, Retrieved May 06, 2020 from
1177 [https://public.wmo.int/en/our-mandate/focus-areas/natural-hazards-and-disaster-risk-](https://public.wmo.int/en/our-mandate/focus-areas/natural-hazards-and-disaster-risk-reduction/tropical-cyclones)
1178 [reduction/tropical-cyclones](https://public.wmo.int/en/our-mandate/focus-areas/natural-hazards-and-disaster-risk-reduction/tropical-cyclones) , 2020.
- 1179 Wong, M. M. F., Fung, J. C. H., and Yeung, P. P. S.: High-resolution calculation of the urban
1180 vegetation fraction in the Pearl River Delta from the Sentinel-2 NDVI for urban climate
1181 model parameterization, *Geoscience Letters*, 6(1), 1-10, [https://doi.org/](https://doi.org/10.1186/s40562-019-0132-4)
1182 [10.1186/s40562-019-0132-4](https://doi.org/10.1186/s40562-019-0132-4), 2019.
- 1183 Xu, S., Zhu, X., Helmer, E. H., Tan, X., Tian, J., and Chen, X.: The damage of urban vegetation
1184 from super typhoon is associated with landscape factors: Evidence from Sentinel-2
1185 imagery, *International Journal of Applied Earth Observation and Geoinformation*, 104,
1186 102536, <https://doi.org/10.1016/j.jag.2021.102536>, 2021.
- 1187 Yang, Q., Qin, Z., Li, W., and Xu, B.: Temporal and spatial variations of vegetation cover in
1188 Hulun Buir grassland of Inner Mongolia, China, *Arid Land Research and Management*,
1189 26(4), 328-343, <https://doi.org/10.1080/15324982.2012.709215>, 2012.
- 1190 Yang, Y., Erskine, P. D., Lechner, A. M., Mulligan, D., Zhang, S., and Wang, Z.: Detecting
1191 the dynamics of vegetation disturbance and recovery in surface mining area via Landsat
1192 imagery and LandTrendr algorithm, *Journal of Cleaner Production*, 178, 353-362,
1193 <https://doi.org/10.1016/j.jclepro.2018.01.050>, 2018.
- 1194 Yin, J., Yin, Z., and Xu, S.: Composite risk assessment of typhoon-induced disaster for China's
1195 coastal area, *Natural hazards*, 69(3), 1423-1434, <https://doi.org/10.1007/s11069-013->

1196 [0755-2](#), 2013.

1197 Yoon, W. S., Yoon, S. H., Moon, J. H., and Hong, J. S.: Topographic Variability during
1198 Typhoon Events in Udo Rhodoliths Beach, Jeju Island, South Korea, *Ocean and Polar*
1199 *Research*, 43(4), 307-320., 2021.

1200 Yu, J. J., Kim, D., and Yoon, J.: A Study on the Short-term Morphological Beach Changes of
1201 Pado-ri Using UAS-based DEM: Focusing on before and after Typhoon Soulik, *Journal*
1202 *of the Association of Korean Geographers*, 7(3), 303-317, 2018.

1203 Yum, S. G., Wei, H. H., and Jang, S. H.: Estimation of the non-exceedance probability of
1204 extreme storm surges in South Korea using tidal-gauge data, *Natural Hazards and Earth*
1205 *System Sciences*, 21(8), 2611-2631, <https://doi.org/10.5194/nhess-21-2611-2021>,
1206 2021.

1207 Zhang, X., Wang, Y., Jiang, H., and Wang, X.: Remote-sensing assessment of forest damage
1208 by Typhoon Saomai and its related factors at landscape scale, *International Journal of*
1209 *Remote Sensing*, 34(21), 7874-7886, <https://doi.org/10.1080/01431161.2013.827344>,
1210 2013.

1211 Zhang, J., Zhang, Z., Chen, J., Chen, H., Jin, J., Han, J., ... and Wei, G.: Estimating soil salinity
1212 with different fractional vegetation cover using remote sensing, *Land Degradation &*
1213 *Development*, 32(2), 597-612, <https://doi.org/10.1002/ldr.3737>, 2021.

1214 Zhang, Y., Sun, Y., Hu, Z., Bian, S., Xiong, C., Liu, J., ... , and Zhang, W.: Increase in
1215 Suspended Sediment Contents by a Storm Surge in Southern Bohai Sea, China,
1216 *Mathematical Problems in Engineering*, 2022, <https://doi.org/10.1155/2022/9585386>,
1217 2022.